Correlation Fourier Diffractometry: 20 Years of Experience at the IBR-2 Reactor

A. M. Balagurov, I. A. Bobrikov, G. D. Bokuchava, V. V. Zhuravlev, and V. G. Simkin

Frank Laboratory of Neutron Physics, Joint Institute for Nuclear Research, Dubna, 141980 Russia
e-mail: bobrikov@nf.jinr.ru

Abstract—The high-resolution Fourier diffractometer (HRFD) was commissioned at the IBR-2 pulsed reactor at FLNP JINR in 1994. The specific feature of the HRFD design is the use of fast Fourier chopper for modulating the primary neutron beam intensity and the correlation method of diffraction data acquisition. This allowed to reach with HRFD extremely high resolution ($\Delta d/d \approx 0.001$) over a wide range of interplanar spacings at a relatively short flight path between chopper and sample ($L = 20$ m). Over time, a lot of diffraction experiments on crystalline materials, the main goal of which was to study their atomic and magnetic structures, were performed at HRFD. Successful implementation of the Fourier diffractometry technique at the IBR-2 reactor stimulated the construction of yet another Fourier diffractometer intended for internal mechanical stress studies in bulk materials (FSD, Fourier Stress Diffractometer). In this paper the experience of using this technique at the IBR-2, which is a long-pulse neutron source, is considered, the examples of HRFD studies are given, and possible solutions for existing technical problems of using correlation diffractometry and ways of increasing the intensity and resolution of HRFD are discussed.

1. INTRODUCTION

Since the start of the first diffraction experiments at nuclear reactors (C. Shull, E. Wollan, 1948–49), gradual specialization of neutron diffractometers has led to the emergence of about ten varieties, each quite different depending on the type of a source, the method of reciprocal space scanning, and optimization for a given parameters. The diffractometers for structural experiments on powders, among which one can distinguish a group of high-resolution diffractometers (still few in number), are probably mostly used.

The resolution of a diffractometer, along with its neutron flux, is the most important parameter that in many respects defines the type of experiments performed with it. According to this parameter, the neutron diffractometers for polycrystals can, to some extent of convention, be divided into three categories: low ($\Delta d/d \approx 0.01$), medium ($\Delta d/d \approx 0.003$) and high ($\Delta d/d \approx 0.001$) resolution (here d is interplanar spacing, Δd is the diffraction peak width). A structural analysis of simple compounds with high symmetry and small volume of a unit cell ($V_c \approx 100$ Å^3) is possible for low resolution. A roughly threefold higher resolution allows one to confidently analyze low-symmetry structures with the unit cell volume up to $V_c \approx 300$ Å^3 and determine the thermal factors in the isotropic approximation. The high resolution makes it possible to analyze structures with $V_c \approx 1000$ Å^3 and higher, the thermal factors can be defined more accurately in the anisotropic version, and the structure of a polycrystal can be determined ab initio.

The ideas of achieving high resolution on a diffractometer with monochromatic beam (λ_0-diffractometer) are well known [1]: it is essential to use a large angle ($\theta_M > 120$ deg) of reflection from a monochromator with small mosaicity, a good beam collimation before the monochromator, and good position resolution of a detector. These principles are used in the design, for example, of the diffractometers D2B (ILL) [2] and HRPT (PSI) [3] running at steady state neutron sources in which $\Delta d/d$ in the minimum of the resolution curve is ~0.0005 and 0.001, respectively.

A time-of-flight (TOF) method is used at pulsed neutron sources with short pulse based on proton accelerators with heavy metal target (these were called spallation neutron sources and further are referred to as spallation sources). In this case, a high resolution of the TOF diffractometer is reached when a relatively thin moderator is employed and the flight path L is more than 50 m. The most famous example is HRPD (RAL) [4] with $L \approx 100$ m and very high nominal resolution ~0.0004, which in addition is weakly dependent on d_{hkl}.

At long-pulse sources, such as IBR-2, now in operation at JINR, Dubna, with $\Delta t_0 \approx 340$ μs [5] and ESS, under construction, with $\Delta t_0 \approx 2500$ μs [6], for reaching high resolution it is necessary to reduce the pulse length by using a particular type of mechanical chopper. In practice, three kinds of fast disc choppers are used: single-slit (Disc Chopper, DC), multi-slit with random arrangement and width of slits (Pseudo-Random Chopper, PRC), and multi-slit with regular arrangement and the same slit width (Fourier Chopper, FC).

With single DC, a standard time-of-flight method is implemented, i.e., planning of experiment and the diffraction data acquisition method are not different from those in the TOF diffractometer case at a short-pulse neutron source. For a source with a very long pulse, more efficient schemes are associated with multiplexing in repetition frequency or in operating range of wavelengths [7]. The PRC and FC choppers suppose a correlation analysis of signals from the chopper and detector. Each of these options has its positive and negative features and, therefore, its specific applications.

In the present paper, we discuss the results obtained during 20 years' operation of the high-resolution Fourier diffractometer (HRFD) running at the IBR-2 reactor. We briefly present the basic principles of the Fourier diffractometry of crystals, including the history of this method. We also consider the emerging technical problems and their possible solutions, as well as new ideas to increase the luminosity and resolution of the diffractometer and to improve the method of experimental data acquisition. Their implementation can turn Fourier diffractometry into the most promising method allowing one construct on a long-pulse neutron source a high-intensity diffractometer with ~0.0003 resolution.

2. CORRELATION METHODS IN NEUTRON DIFFRACTOMETRY

A high resolution of the $\Delta d/d \approx$ flight 0.001 level can be relatively easily achieved at spallation sources (ISIS, J-PARC, SNS) by using the conventional time-of-flight method when the flight path exceeds 70 m. Indeed, the time component of the resolution function is $(\Delta d/d)_{\mathrm{TOF}} = \Delta t/t$, where $t = 252.778 \times L\lambda$ is the total neutron time of flight between a source and a detector (here the time is in μs; path, in meters; and wavelength, in Ångström units). If $(\Delta t_0)_{\mu s} \approx 15 \times \lambda$ Å, which is typical for spallation sources, then $(\Delta d/d)_{\mathrm{TOF}} \approx 0.00085$ for $L = 70$ m and is independent of the neutron wavelength to a first approximation. Assuming the same contribution to the resolution function from geometrical uncertainties and quadratically adding both terms, we get $\Delta d/d \approx 0.0012$.

The main drawbacks of the TOF diffractometers with large flight path are intensity losses in a long neutron guide and too small d_{hkl} range attainable at fixed scattering angle. The latter is due to overlap of the spectra generated by successive pulses, which is especially significant for sources with high repetition frequency, for example, 50 Hz (ISIS) or 60 Hz (SNS). Thus, for the diffractometer HRPD (ISIS) with $L \approx 100$ m at large scattering angles, the observable d_{hkl} range is only 0.4 Å and, to extend it by at least 2 Å, it is necessary to remove 4 of 5 pulses with the help of additional choppers, i.e., to work with five times reduced intensity.

This problem can easily be overcome by using the correlation technique of diffraction data acquisition and PRC [8] or FC [9] choppers, because in this case the very idea of the method provides for spectra overlap. In addition, with their help it is possible to attain a high resolution for a relatively short flight path. After trial implementation of the correlation techniques at nuclear reactors (see, for example, [10, 11]), the prospect for their usage seemed rather high, but for some reasons both techniques have never received wide acceptance. For continuous-operation neutron sources, their application is hampered due to high correlation background, which is proportional to the total number of detected neutrons at each point of the diffraction pattern. At short pulse spallation sources ($\Delta t_0 \approx 20$–50 μs), the construction of which began in the 1980s, TOF diffractometers with the flight path $L \approx 50$–100 m, despite the mentioned drawbacks, proved to be quite successful tools, and the necessity of introducing distinctly more complicated (both technically and conceptually) correlation techniques turned questionable.

Nevertheless, the potentialities of the correlation techniques are high, and this is particularly true for the Fourier method, by which it is possible to achieve an optimal balance between intensity and resolution. The most promising way is to use the Fourier diffractometer at a high-flux long-pulse ($\Delta t_0 > 300$ μs) source. Although currently there is only one such neutron source (the IBR-2 pulsed reactor in Dubna), the construction of ESS started recently ($\Delta t_0 \approx 2500$ μs) suggests that it is long-pulse spallation sources that will be built in the future. For this there are economic reasons (the long-pulse spallation source lacks a proton storage accelerator, the most expensive device), as well as the desire appreciably to increase the average power of the source (heat load on the target becomes much smaller as the pulse lengthens).

3. FOURIER DIFFRACTOMETRY OF CRYSTALLINE MATERIALS

When using any type of choppers (DC, PRC or FC), the dependence of the intensity of neutrons scattered by crystal and captured by detector on time, t, and chopper rotation frequency, ω, can be expressed by the formula

$$I(\omega, t) \sim \int \sigma(\tau) \mathrm{T}[(\tau - t), \omega]\mathrm{d}\tau, \qquad (1)$$

where $\sigma(t)$ is the elastic cross section of scattering of neutrons by crystal; t is the time of flight between a chopper and a detector which is easily related to the neutron energy, transferred momentum, and interplanar spacing; $\mathrm{T}(t, \omega)$ is the chopper transmission at the rotation frequency ω. The transmission function is defined by chopper design, and the task is to select a specific $\mathrm{T}(t)$ needed for determining the scattering cross section $\sigma(t)$ manifested for crystals as a set of
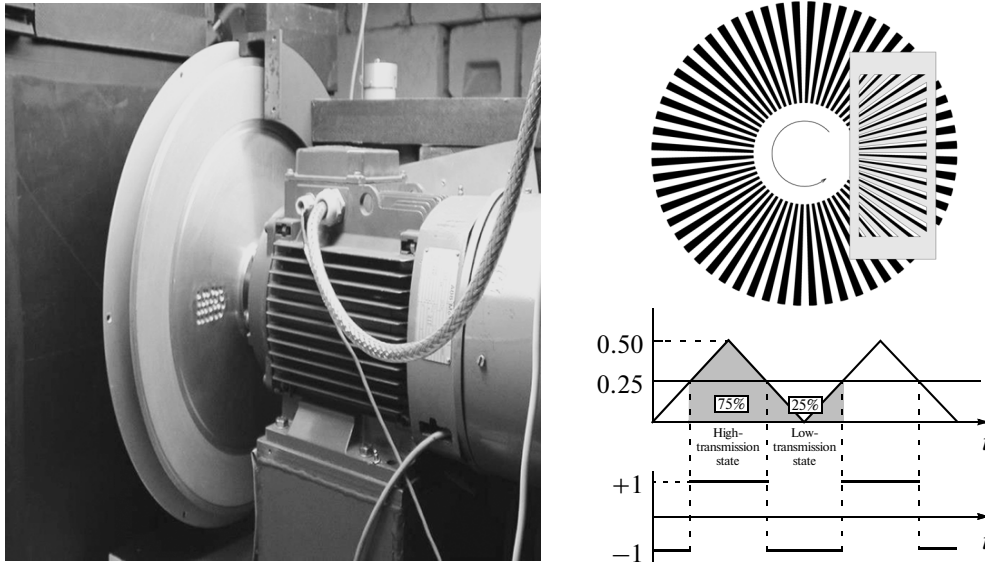
Fig. 1. A photo of the Fourier chopper of HRFD (left). One can see a disk (rotor) of the chopper (part of the casing is removed), whose outer circumference is a system of transparent and opaque gaps to thermal neutrons, and an electromotor to the axis of which it is attached. To the right are schematically represented rotor and stationary stator. The diagram below shows a saw-tooth function of transmission of this system and its approximating sequence of positive and negative binary (pick-up) signals.

narrow Bragg peaks, which allows comparative ease separating them from the background.

For the three listed types of chopper, $T(t, \omega)$ can, with some certainty, be presented in the following way. The DC rotates with fixed frequency and if it is large enough, then $T(t, \omega) \sim \delta(t)$ and from (1) it follows that $I(t) \sim \sigma(t)$.

For the PRC (which also rotates at large and fixed frequency), $T(t)$ is selected as a random function such that $\int T(t - t') \times T(t' - \tau) dt' \sim \delta(t - \tau)$, i.e., the autocorrelation function should be as sharp as possible. In this case the convolution of $I(\omega, t)$ with $T(t, \omega)$ allows one to determine $\sigma(t)$. Since $T(t, \omega)$ cannot be truly random (at least because it repeats with a period of rotation), it is common practice to call this technique as pseudorandom one.

Finally, the FC has a periodic transmission function and, if $T(t, \omega)$ were an ideal sinusoid, then at fixed rotation frequency of the chopper the intensity of scattered neutrons would be a Fourier harmonic of scattering cross section, namely, $I(\omega) \sim \int \sigma(\tau) \sin(\omega \tau) d\tau$. Measuring $I(\omega)$ over a wide frequency range, we can reconstruct the Fourier transform, i.e., obtain the scattering cross section $\sigma(t)$.

In practice, the expressions for $T(t, \omega)$ discussed above are to a large extent approximate and the determination of exact $\sigma(t)$ dependence involves several restrictions. For DC this is the finite width of transmission function directly affecting the resolution and luminosity of the diffractometer. One of the main

problems of using DC is a limitation on the cross section of the primary neutron beam, which leads to the necessity of using small volume samples. The FC transmission function cannot be purely sinusoidal, at least because intensity modulation is possible only in the range from zero to unity. As a result, in the intensity of the neutrons registered by the detector there appears a background component proportional to the total number of scattered neutrons which is usually called the correlation background.

3.1. Some Historical Moments of Fourier Diffractometry Evolution

The general principles of neutron Fourier diffractometry have been known since 1968 [12, 13]. In this technique, the neutron beam intensity on a sample is modulated by a fast Fourier chopper (Fig. 1), which is a rotating disc (rotor) with gaps transparent and opaque for thermal neutrons and evenly spaced around the circumference and a fixed system of similar gaps (stator). In the ideal case, the Fourier chopper transmission is independent of the number of slits and makes 1/4 of the total neutron flux, which is much higher than in the DC case. At the same time, the Fourier chopper can provide a sufficiently small neutron pulse width due to the narrowness of the slits and large rotation frequency and, hence, a high resolution.

The original idea of employing the Fourier chopper, which was realized for a diffraction experiment with single crystal in papers [14, 15], was to measure intensity at four points of the chopper transmission curve with a few properly selected rotation frequen-

cies. The combination of the measured intensities theoretically allowed for reconstructing the crystal scattering cross section. The calculations proved that in diffraction experiments the Fourier chopper, combined with a multidetector recording system, would increase the reactor neutron efficiency a hundred times or more as compared to the conventional diffractometers existing at that time. The technical problems associated mainly with the need for high degree stabilization of the chopper rotational velocity prevented this idea from being implemented in its original form.

The Fourier diffractometry became distinctly feasible in the early 1970s, after a new method for detecting scattered neutrons, now known as the reverse time-of-flight (RTOF) one, had been developed by Finnish physicists [16, 17]. The first RTOF Fourier diffractometer ASTACUS was commissioned already in 1974 at the reactor in VTT Technical Research Centre of Finland (Espoo), which was reported at the Neutron Diffraction Conference in 1975 [18]. Despite insufficient luminosity (the reactor power in Espoo was only 250 kW), the diffraction pattern from oriented graphite blades were measured and the main advantage of the Fourier method—high resolution at comparatively short flight path—was verified ($\Delta d/d \approx 0.002$ was obtained for $L = 8.56$ m).

This success encouraged constructing Fourier diffractometers at steady-state reactors at PNPI (Gatchina) (mini-SFINKS, [19]) and GKSS (Geesthacht, Germany) (FSS, [20]). The PNPI diffractometer with $\Delta d/d \approx 0.002$ was oriented to structural studies, the diffractometer at GKSS with $\Delta d/d \approx 0.004$ was optimized for internal stress studies in bulky products and materials. Methodical work with a large body of research aimed at testing the general principles of RTOF diffractometry and new ideas for improving the method was performed with both diffractometers. Of most importance were studies into the factors affecting the shape of diffraction peaks measured with the Fourier diffractometer, which were performed by V.A. Kudryashev with co-authors [21, 22].

At the development stage of the RTOF method, it became clear that it can be used at both steady-state and pulsed neutron sources. Moreover, the pulsed character of the source allows an additional gating of detected signals (see subsection 3.3) and appreciably reduces the correlation background, thus increasing the efficiency of the diffractometer. In Europe, the pulsed neutron source was already in operation in the mid-1980s. It was the high-flux pulsed reactor IBR-2 [23] at JINR (Dubna), with pulse length (350 µs) optimal for Fourier diffractometry. A group of Finnish physicists led by P. Hiismäki theoretically substantiated the exploitation of the Fourier method on a pulsed source [24] and forwarded a proposal to implement this idea to JINR in late 1986. The proposal was accepted and a joint JINR (Dubna)—PNPI (Gatchina)—VTT (Espoo) project started. The project was financed by the State Scientific—Technical Program "High-Temperature Superconductivity" set up in 1987, and by JINR.

The basic equipment for the new facility, called the high-resolution Fourier diffractometer (HRFD), was constructed in Espoo (correlation electronics and Fourier chopper with control system) and PNPI (mirror neutron guide and detector). Neutron beam line and software were the responsibility of FLNP JINR. Irregular funding caused some delay in delivery of complete equipment, but by the mid-1992 a prototype version of the diffractometer was constructed and first diffraction pattern were measured, which was reported in [25]. Full assembly of HRFD was complete by 1994, and then its regular operation and implementation of the scientific program began [26]. In particular, the first work in which new scientific data were obtained employing HRFD was a structural study of high-temperature superconductor $YBa_2Cu_4O_8$ (Y-124), with 10% yttrium substituted for calcium [27].

The internal stress study in bulky products (see, for example, [28]) has become one of the most dynamic research areas at HRFD. Therefore, in late 1990s it was decided to construct at IBR-2 another Fourier diffractometer, optimized for solving such problems. The development of the facility, called the Fourier stress diffractometer (FSD), was performed jointly with the specialists of PNPI (Gatchina). The experience gained during the creation of HRFD and in the course of its operation helped to manufacture rather quickly all the major FSD units, and to report on the commissioning in 2002 [29].

The program of constructing neutron spectrometers for the new spallation source ESS included Fourier diffractometry as an alternative to other methods of achieving an optimal combination of extremely high resolution and high luminosity [30].

3.2. Fourier Diffractometer at Pulsed Neutron Source

In the RTOF method, the saw-tooth function of modulation in its simplest form is approximated by a sequence of binary signals (pick-up signals) generated by a encoder connected with the chopper's rotor (Fig. 1). Assuming that the neutron scattering by the sample is elastic, we can define the state of the Fourier chopper at any moment prior to registration of a neutron by the detector (Fig. 2). In the first version of the electronics for RTOF diffractometers, the storage of the information in the operating memory of the multichannel analyzer was realized by using a shift register (digital delay line), to which a pick-up signal was supplied; transfer of information to the memory was accomplished on a signal from the detector. Unity was added to the memory cells that corresponded to the positive level of the pick-up signal. When implementing
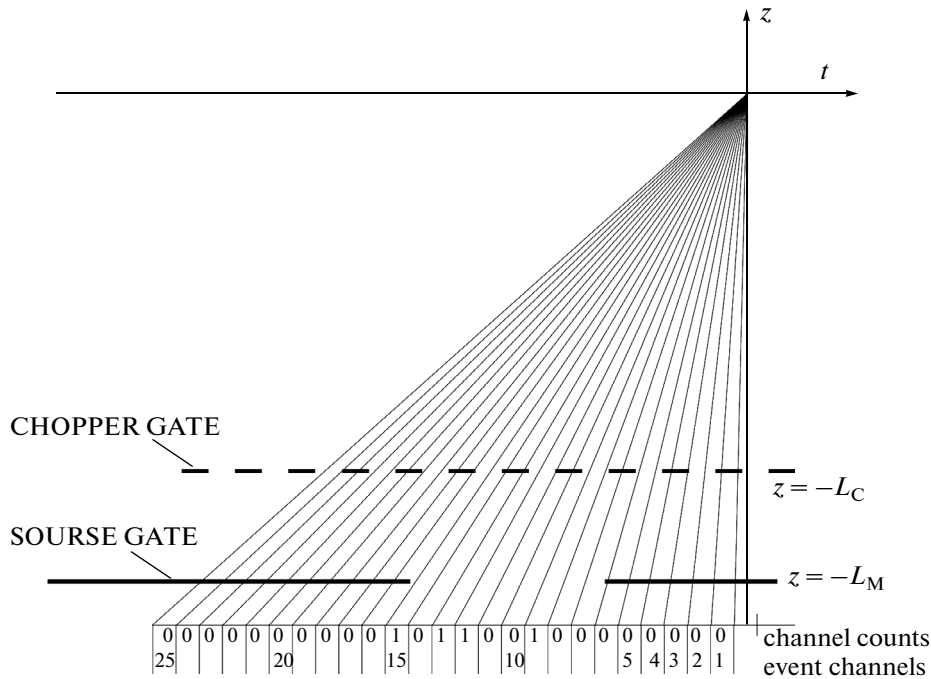
Fig. 2. A scheme of the event classification in the RTOF method at a pulsed neutron source. At the bottom are the time analyzer channels, containing 1, when the neutron path $z(t)$ from the source (at $z = -L_M$) through the chopper (at $z = -L_C$) to the detector (at $z = 0$) passes through "open" states of the source and chopper, corresponding to the state +1 of the sequence of binary signals at the bottom of Fig. 1.

the RTOF method on a pulsed neutron source, additional gating of memory is performed by a pulse synchronized with the source power pulse (line $z = -L_M$ in Fig. 2). Correspondingly, unity is added to the analyzer memory cell if and only if both the neutron source and the chopper are in the "open" state for the line $z(t)$ on the diagram.

A detailed and mathematically rigorous description of this process for a pulse source is given, for example, in papers [17, 24], where it is shown that, in the case of continuous variation of the Fourier chopper's rotation frequency from 0 to some maximum frequency ν_{max}, the intensity of neutrons elastically scattered by a crystalline sample (and measured by the detector) as a function of the time of flight t can be presented in the form

$$I(t) \sim \pm \int R_s(t-\tau)R_c(t-\tau)\sigma(\tau)d\tau$$
$$+ c \int R_s(t-\tau)\sigma(\tau)d\tau + B(t), \qquad (2)$$

where R_s is the function describing the neutron pulse from the source, R_c is the resolution function of the Fourier chopper, σ is the elastic diffraction scattering cross section, B is the normal background, c is a constant close to unity. The function R_s is a gating pulse with width corresponding to the width of the source

power pulse (340 μs for the IBR-2 reactor). It can be shown that for R_c the following expression holds:

$$R_c(t) \approx \Omega^{-1} \int_0^{\Omega} g(\omega)\cos(\omega t)d\omega, \qquad (3)$$

where $g(\omega)$ is the rotation frequency distribution function and Ω is the maximum frequency of neutron beam modulation by the Fourier chopper. If the chopper's maximum rotation frequency is ν_{max} and the number of slits on the chopper is N, then $\Omega = 2\pi N \nu_{max}$. The width $R_c(t)$ depends on the form of the function $g(\omega)$ but is mainly defined by Ω, namely, $W_c \approx 2\pi/\Omega$. For instance, for $\nu_{max} = 150$ Hz and number of rotor slits 1024 (the parameters of HRFD Fourier chopper) we have $\Omega/2\pi \approx 150$ kHz. This quantity defines the efficient pulse width provided with the help of the Fourier chopper; i.e., in this case the δ-shaped distribution $\sigma(t)$ will be transformed into the function $R_c(t)$ with a width at half maximum of $W_c = \Delta t_0 \approx 7$ μs.

As the distribution width $R_c(t)$ is substantially smaller than the width $R_s(t)$, $W_c \ll W_s$, the first term in the expression (2) is narrow diffraction peaks of width close to W_c (for a perfect crystal $\sigma(t)$ consists of a sum of δ-shaped Bragg peaks). The second term in (2), which may be called "correlation background", corresponds to the same Bragg peaks but their width is close
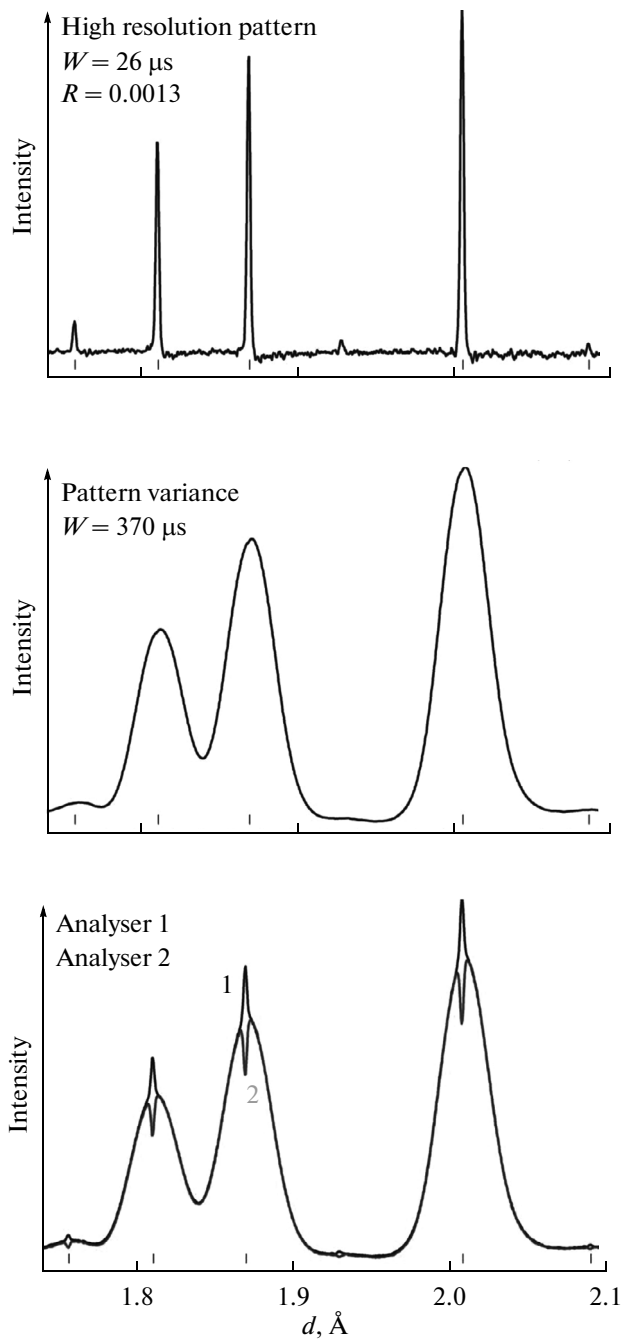
Fig. 3. A section of the neutron-diffraction pattern of the powder $Na_2Al_2Ca_3F_{14}$ (NAC) in the range of interplanar spacings $d = 1.74–2.10$ Å with several closely spaced strong and weak diffraction peaks. The spectra shown at the bottom are measured in parallel by two analyzers and contain broad and narrow (positive and negative) peaks. The sum of counts of the analyzers (middle plot) gives dispersion for the high-resolution spectrum produced when subtracting spectrum 2 from spectrum 1 (upper plot). The width of a peak in the dispersion spectrum ($W = 370$ μs) approximately corresponds to the pulse width of the neutron source, the width of the high-resolution peaks ($W = 26$ μs) corresponds to the diffractometer resolution function ($R = 0.0013$). Positions of the diffraction peaks for NAC are indicated. The small peak at $d \approx 1.935$ Å corresponds to the impurity phase.

to W_s, i.e., the overall picture represents a background with narrow peaks on top of broad peaks.

This picture can be simplified by collecting the diffraction data into two independent memories with a π phase shift of pick-up signal from the Fourier chopper. Formally, this operation corresponds to control of the sign (plus or minus) before the first term in (2). Accumulating concurrently the functions $I(t)_+$ and $I(t)_-$ and finding the difference $[I(t)_+ - I(t)_-]$, we can obtain a high resolution diffraction pattern without the presence of broad peaks from the source (Fig. 3). In this case, the sum $[I(t)_+ + I(t)_-]$ yields, to a good accuracy, a dispersion of counting rate in a high-resolution spectrum.

When operating the stationary neutron source, the structure of the expression (2) remains the same, but $R_s(t)$ should be replaced with a constant. In this case, the first term is, as before, a set of narrow diffraction peaks; the second term (correlation background) becomes a constant whose magnitude is proportional to the total intensity of neutrons scattered by a crystal.

3.3. Qualitative Analysis of Fourier Chopper Operating on Pulsed Neutron Source

The mathematical model for data registration when working with the Fourier chopper, which is based on Fourier transforms of the chopper transmission function and its approximating sequence of electronic signals, allows us to derive formulas for the intensity of diffraction peaks, its dispersion and correlation background. But from this model we cannot understand how the narrow diffraction peaks are formed at the saw-tooth modulation of intensity of the neutron beam incident on a crystal, why a background component emerges, or why the correlation background decreases when working at a pulsed neutron source. Below we give qualitative answers to these questions.

First we consider the operation of the Fourier chopper at a steady-state source of neutrons. In this case, in Fig 2, there is no source gate; i.e., the source is always in the "open" state. When the Fourier chopper rotates at a certain frequency and a neutron is counted by detector, unity is added to all memory cells corresponding to the neutron paths $z(t)$ passing through the "open" states of the chopper. The same happens at any other chopper rotation frequency. But to the elastic diffraction cross section of the crystal there correspond only some strictly defined paths $z(t)$. For instance, if the neutrons are scattered by a family of crystallographic planes of a single crystal, then only a few orders of reflection of neutrons must be observed. Their times of flight for the chopper–crystal–detector path (L) satisfy the relationship $t_n = t_1/n$, t_1 is the time-of-flight of neutrons for the 1st order of reflection ($t_1 = 505.556 \times L d_{hkl} \sin\theta$, θ is the Bragg angle), n is the number of order of reflection. Accord-
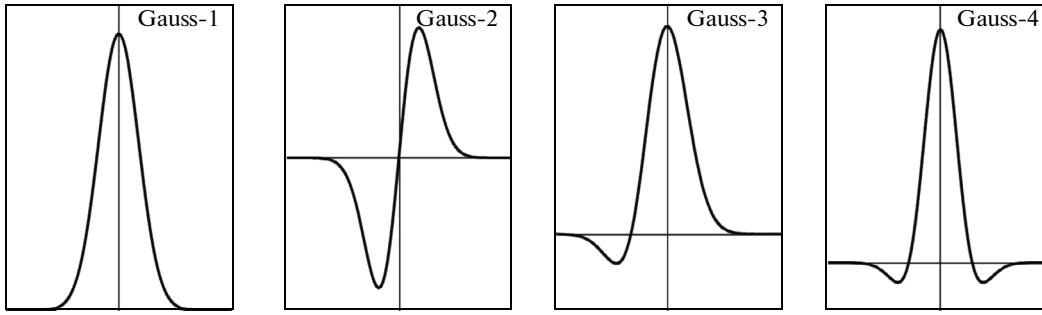
Fig. 4. The time component of the resolution function of the diffractometer $R_c(t)$ for the cases (a) $\varphi_0 = 0$ and $\delta = 0$, (b) $\varphi_0 = \pi/2$ and $\delta = 0$, (c) $\varphi_0 = 0$ and $\delta > 0$, (d) $\varphi_0 = 0$ and $\delta = 0$ and the contribution of low frequencies to the Gaussian distribution $g(\omega)$ is reduced.

ingly, in the given range of the time-of-flight there will be only a few paths $z(t)$ which, regardless of the rotation frequency of the chopper, always pass through its "open" state and for which unity will be added to the memory cell for each detector hit. For any other paths, addition of unity will depend on the chopper rotation frequency, i.e., it is statistical. Thus, during the time the chopper passes a frequency range from 0 to ν_{max}, all memory cells will accumulate some statistical fluctuating intensity ("correlation background") and the cells that correspond to the positions of orders of reflection on the time-of-flight scale will gain extra intensity (diffraction peaks) proportional to the scattering cross section for each specific order.

With Fourier chopper operating at a pulsed neutron source, analysis is added of the correspondence of the paths $z(t)$ to the "open" state of the source, which is modeled by an additional gating pulse of required length (350 μs for IBR-2). As a result, the correlation background is formed only in a small neighborhood of the diffraction peaks and its profile is close to the profile of the diffraction pattern measured without the Fourier chopper. The main effect is that the correlation background level becomes proportional to the intensity of a specific diffraction peak and, of course, it is much smaller than in the first case, where the background level is proportional to the total number of the events registered by the detector.

From this consideration it is also clear that the width of high-resolution peaks will be inversely proportional to the maximum rotation frequency of the Fourier chopper because with increasing frequency the uncertainty of assigning an event of the detector to a particular memory cell decreases.

3.4. The Diffraction Peak Profile

A comprehensive analysis of the factors affecting the resolution function that defines the diffraction peaks measured with the Fourier diffractometer is presented in two papers by V.A. Kudryashev with co-authors [21, 22]. In particular, they derived formulas for the time component of the resolution function of the diffractometer, $R_c(t)$, for several different distribution functions of rotation frequencies FC ("frequency windows"), $g(\omega)$, and established the reasons why the peak profile deviates from the expected one.

Formula (3) is true in the absence of mismatch between the saw-tooth function of transmission and a sequence of binary pick-up signals. A more general consideration [22] results in an expression that includes a phase shift φ_0 between these functions (the principal cases: $\varphi_0 = 0$ and $\pi/2$) and a random deviation from φ_0 (phase error, δ). Figure 4 shows several practically important variants of the time component of the resolution function mainly determining the diffraction peak profile. At $\varphi_0 = 0$ and $\delta = 0$ the function $R_c(t)$ is symmetric with respect to $t = 0$ and is close in form to the Gaussian, while at $\varphi_0 = \pi/2$ and $\delta = 0$ it is antisymmetric and close in form to the first derivative of the Gaussian. Nonzero phase error, $\delta \neq 0$, leads to asymmetry in the profile of the peak, and with reduced contribution of small modulation frequencies there arise dips on both sides of the maximum.

The influence of the geometrical factors on the peak profile leads as a rule to its broadening. In the simplest case, dispersions of time and scattering angle distribution functions are added, with the peak profile remaining unchanged or changing only slightly.

3.5. The Correlation Background

The difference in the form and magnitude of the correlation background is the main factor distinguishing between the Fourier chopper applications at the steady-state and pulsed neutron sources. For a pulsed source it is proportional to the source pulse width and can be approximately presented as an integral of the flux $\Phi(\lambda)$ over the wavelength range equivalent to W_s:

$$B_c \sim \int R_s(t - \tau)\sigma(\tau)d\tau \sim \int_{\Delta\lambda} \Phi(\lambda)d\lambda = \Phi(\lambda)\Delta\lambda. \quad (4)$$

In the case of a steady-state source, the background is independent of the wavelength and proportional to the total number of registered neutrons. Accordingly,
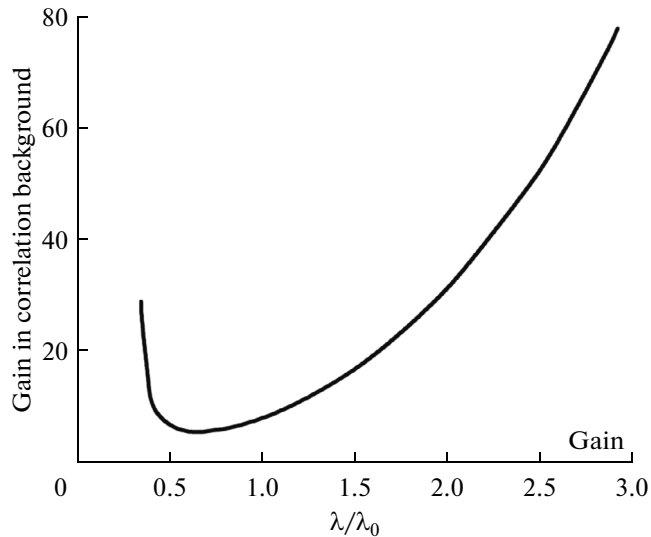
Fig. 5. The ratio of correlation background for the Fourier diffractometer at steady-state and pulsed neutron sources. When calculating B_c by formula (4), the Maxwell distribution of the neutron flux in the wavelength and $\Delta\lambda = 0.02\lambda_0$ were assumed, where λ_0 is the distribution parameter.
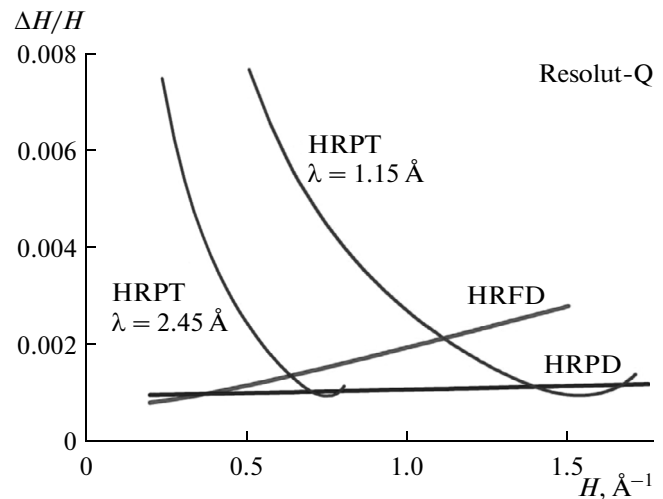

Fig. 6. The resolution functions of diffractometers for polycrystals: two TOF diffractometers (HRFD at IBR-2 and HRPD at ISIS) and λ_0-diffractometer HRPT (SINQ, PSI) for two wavelengths, shown as a function of the vector length in reciprocal space.

we can estimate how much smaller its magnitude for the pulsed source is than for the steady-state one, taking the ratio of the total flux to $\Phi(\lambda)\Delta(\lambda)$ (Fig. 5). It is seen that this effect is quite significant, especially in the low-intensity parts of the spectrum, and it is because of this effect that one can confidently observe low-intensity diffraction peaks at the pulsed source if they do not overlap with strong peaks, as, for example, the peaks for $d \approx 1.769$ Å, 1.935 Å and 2.095 Å in Fig. 3.

More detailed calculations for specific samples showed that the effect is really very significant; for example, for NAC the statistical error in the integral intensity of diffraction peaks decreases ≈ 6 times in the maximum of the Maxwell distribution and ≈ 15 times and more at $\lambda > 4$ Å.

3.6. The Resolution

For the Fourier diffractometer, the resolution $R = \Delta d/d = \Delta H/H$, where d is the interplanar spacing and $H = 1/d$ is the length of vector in reciprocal space, is calculated in the same way as for the conventional TOF diffractometer for powders. The complete expression for calculating $R(d)$ includes three terms:

$$R = \left[(\Delta t_0/t)^2 + (\Delta\theta/\tan\theta)^2 + (\Delta L/L)^2\right]^{1/2}, \quad (5)$$

where Δt_0 is the effective neutron pulse width defined by the maximum frequency of the neutron beam modulation by the Fourier chopper, $t = 252.778 \times L\lambda$ is the total time of flight (in μs), L is the flight path from the Fourier chopper to the detector (in meters), λ is the neutron wavelength (in Å), and θ is the Bragg angle. Limiting the linear dimensions of the sample and

using detectors with a small-thickness registering layer, we can make the contribution of the third term in (5) sufficiently small and consider further only the time and geometrical contributions.

Because obvious relations $t \sim \lambda \sim d \sim 1/H$ hold for the TOF diffractometer, and the effective pulse width for the Fourier diffractometer, Δt_0, is independent of wavelength, $\Delta t_0/t \sim 1/d \sim H$. For short-pulse pulse spallation sources the relation $\Delta t_0 \sim \lambda$, as a rule, holds and the first term in (5), as well as the geometrical component $\Delta\theta/\tan\theta$, is constant to a first approximation. Model calculations of resolution functions of the TOF diffractometer HRPD (ISIS) [4] and Fourier diffractometer HRFD (IBR-2) are shown in Fig. 6. A resolution function of the high-resolution diffractometer with monochromatic beam HRPT (SINQ) [3] for two wavelengths is given for comparison. It is obvious that the resolution functions of HRPD and HRFD have a much weaker dependence on H than in the HRPT case and, moreover, at small H (respectively, large d) the resolution of the diffractometers employing the time-of-flight method is much better than that of monochromatic-beam diffractometers.

4. HRFD—FOURIER DIFFRACTOMETER AT IBR-2 PULSED REACTOR

At IBR-2 reactor (JINR, Dubna), a neutron pulse is formed through a mechanical modulation of its reactivity; for thermal neutrons its duration is around 340 μs and is almost independent of neutron energy. The Fourier diffractometer HRFD was constructed in the early 1990s by a collaboration of FLNP JINR (Dubna), PNPI (Gatchina) and VTT (Espoo, Finland) [25] and
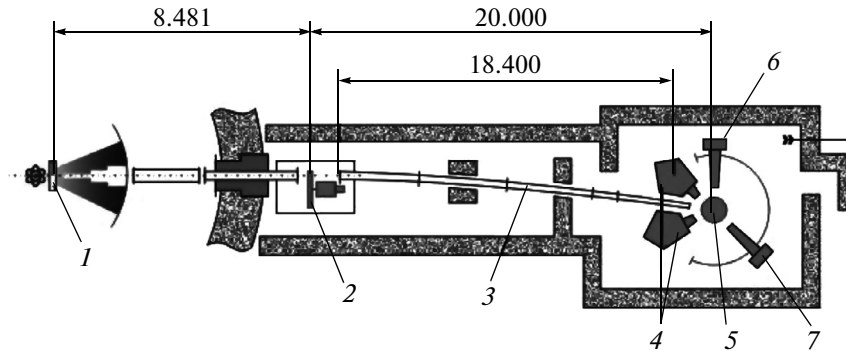
Fig. 7. The configuration of HRFD at the IBR-2 reactor: *1*—water moderator, *2*—Fourier chopper, *3*—curved mirror neutron guide, *4*—backscattering detectors (2θ = ±152 deg), *5*—sample position, *6*—detector at 2θ = 90 deg, *7*—position-sensitive detector at 2θ = 30 deg.

began operating routinely in 1994. It is mainly intended for structure studies of polycrystals; sometimes it serves for experiments on single crystals, if there is a need for high resolution, and experiments related to the analysis of the microstructure of crystalline materials [26].

The original design of HRFD, principle of operation, and parameters are outlined in paper [31]. Modifications extending the potential of HRFD (see, for example, [32]) were repeatedly reported at ICANS conferences. At present, HRFD (Fig. 7) is placed on a beamline equipped with a water comb moderator. In the future this beamline will be supplied with a combined moderator consisting of warm and cold (cooled down to ~30 K) parts. This will ensure an increase of the neutron flux, especially at λ > 4 Å, and its more uniform spectral distribution.

The detection system of HRFD in standard mode allows high-resolution diffraction data acquisition by backscattering detectors ($\Omega_D = 0.16$ sr, 2θ = ±152 deg) in the range of $d_{hkl} = 0.6-3.6$ Å and by the detector at 2θ = 90 deg ($\Omega_D = 0.04$ sr) in the range of $d_{hkl} = 0.8-4.9$ Å. In low-resolution mode (without using correlation analysis) the same detectors register spectra in the ranges of up to 4.5 and 6.0 Å, respectively. Finally, diffraction is observed up to $d_{max} = 16$ Å ($\Delta d/d \approx 0.1$) with the use of a position-sensitive detector (1D PSD) set at 2θ = 30 deg. The detectors at 2θ = ±152 deg and 2θ = 90 deg have been made on the basis of ^{6}Li glasses using the principle of time focusing to minimize the contribution of angular uncertainty (the second term in (5)) to the resolution function. Detailed analysis of optimization of the TOF diffractometer detector system using the geometrical focusing is presented in paper [33], while a special consideration of HRFD can be found in [34]. Examples of diffraction pattern measured with various detectors of HRFD are shown in Fig. 8.

From formula (5) it follows that the width of diffraction peaks as a function of the interplanar spacing can be written in the form

$$W_R^2 = C_1 + C_2 d^2, \qquad (6)$$

where C_1 and C_2 are some constants related to Δt_0 and $\Delta\theta$, respectively. A conventional method for determining their values is a diffraction experiment with polycrystals Al_2O_3, LaB_6 (from the "NIST standards" series), or $Na_2Al_2Ca_3F_{14}$ (NAC), which assumes no microstrain and rather large dimensions of the coherently scattering blocks. With real crystal, according to Williamson−Hall analysis (its state-of-art review, see, e.g. in [35]), the broadening due to the effects of microstrain, ε, and size, L, in the interplanar spacing scale is expressed by the formula $W_\delta^2 = (2\varepsilon d)^2 + (kd^2/L)^2$ when one uses a Gaussian approximation for distribution functions (k is a dimensionless coefficient close to unity which takes into account the shape of coherent blocks). Combining the expressions for W_R^2 and W_δ^2, we get for the diffraction peak's width of the real crystal as a function of interplanar spacing:

$$W^2 = C_1 + (C_2 + C_3)d^2 + C_4 d^4, \qquad (7)$$

where $C_3 \approx (2\varepsilon)^2$, $C_4 \approx (k/L)^2$. The dependences $W^2(d^2)$ will be linear with no size effect (big crystallites) and parabolic in its presence. Accordingly, plotting these dependences in a sufficiently large range of d_{hkl}, we can determine ε and L.

The measured dependences $W^2(d^2)$ for the above standard polycrystals (isotope ^{11}B was used for producing LaB_6) are shown in Fig. 9. We notice that NAC, with all points fitting a linear dependence rather well, i.e., with no size effect and noticeable anisotropy in peaks broadening, is best suited for determining the resolution function. A slight microstrain effect arises for LaB_6, and the size effect develops for Al_2O_3. The
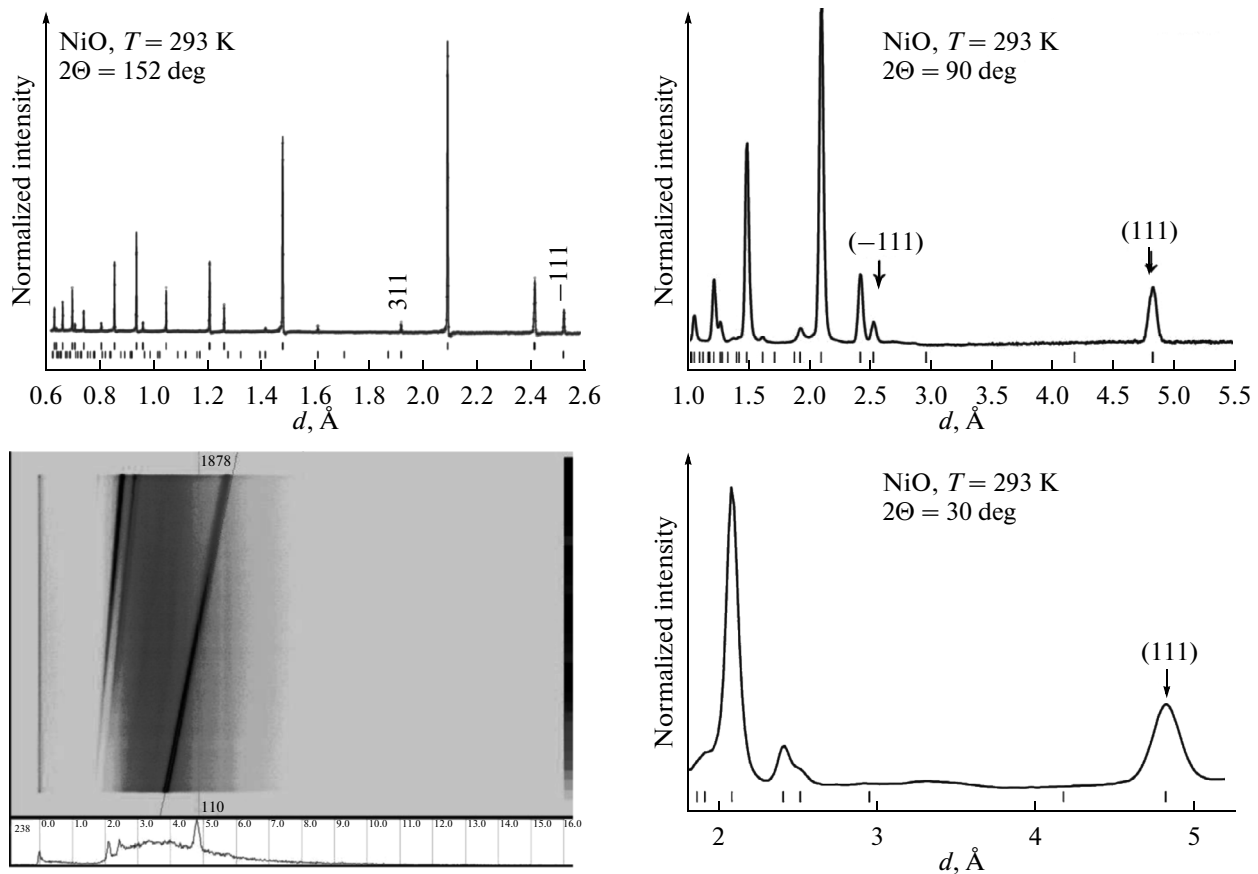
Fig. 8. The diffraction pattern of NiO in the antiferromagnetic phase, measured by different detectors of HRFD. Top left: high resolution—the detectors at $2\Theta = 152$ deg, the result of the processing by the Rietveld method is shown, the vertical bars indicate the calculated positions of the diffraction peaks of the crystalline (upper row) and magnetic (lower row) phases. Top right: low resolution—the detector at $2\Theta = 90$ deg, the Miller indices of the first magnetic peaks are shown. Bottom left: low resolution—PSD at $2\Theta = 30$ deg, 2D representation, the axes correspond to the time of flight (horizontal) and scattering angle (vertical). Bottom right: a spectrum measured by PSD after summation along the lines $\lambda = 2d\sin\theta$ and normalization, the Miller indices of the first magnetic peak are indicated.
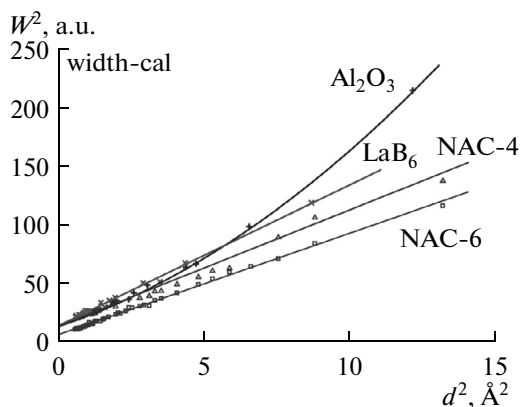
Fig. 9. The dependences $W^2(d^2)$ for Al_2O_3, LaB_6 (NIST standards) and NAC. The experimental points are obtained at the Fourier chopper maximum velocity 4000 rpm (Al_2O_3, LaB_6 and NAC-4) and 6000 rpm (NAC-6). The dependences for LaB_6 and NAC are linear whereas for Al_2O_3 a size effect ($L \approx 3140$ Å) is seen.

resolution function, $R = \Delta d/d$, plotted on the basis of NAC data is shown in Fig. 10.

The intensities of diffraction peaks measured on HRFD are described by formulas that are valid for the conventional TOF diffractometer, and for their analysis we can use the Rietveld method. Namely, the profile of a diffraction pattern as a function of interplanar spacing is

$$I(d) \sim \Phi(d)A(d)\sum_{hkl}j_{hkl}\left|F(\mathrm{H}_{hkl})\right|^2$$
$$\times Q_L\varphi(d_{hk1} - d) + \mathrm{B}(d),$$
(8)

where $\Phi(d)$ is the effective spectrum of neutrons incident on a sample, which includes corrections for neutron transmission on flight paths and the detector efficiency; $A(d)$ is the neutron absorption factor (the extinction coefficient can also be included here); j_{hkl} is the multiplicity factor for a plane (hkl); $F(\mathrm{H}_{hkl})$ is the structural factor for a site (hkl) of reciprocal lattice;
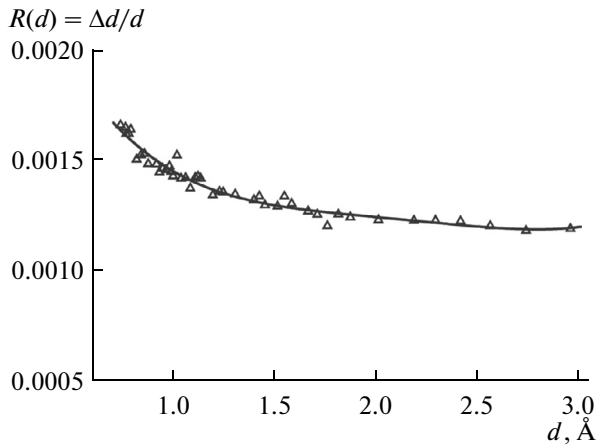
Fig. 10. HRFD resolution function obtained from the data for $Na_2Al_2Ca_3F_{14}$ (NAC) at the Fourier chopper maximum velocity 6000 rpm. The line is guide for the eyes.
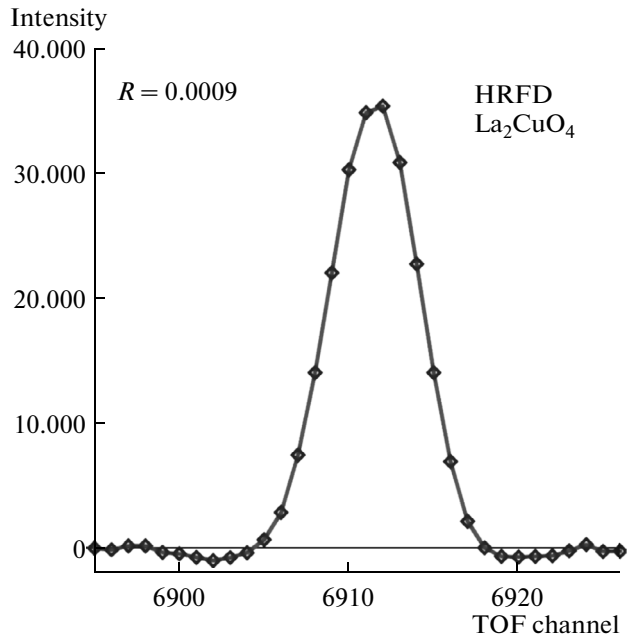

Fig. 11. A typical diffraction peak measured on a single crystal La_2CuO_4 at 6000 rpm and the width of analyzer channel 2 μs. The relative width of this peak is $\Delta d/d = 0.0009$. The small negative dips on both sides of the peak are due to the correlation data acquisition method.

$Q_L = \lambda_0^4/(2\sin^2\theta_0)$ is Lorentz factor; λ_0 and θ_0 are the wavelength and Bragg angle for which the diffraction peak (hkl) is measured; $\varphi(d_{hkl} - d)$ is the function describing the profile of a diffraction peak (for a sample with no microstrain and with big crystallites, φ coincides with the resolution function); B(d) is the background intensity. As usual, the function (8) is parameterized and refinement of the parameters is done using the least square method. This procedure and the experimental or calculated determination of correction functions are outlined, for example, in [36].

In reality, the situation is somewhat complicated by the fact that for high intensity deviations of the profile of measured diffraction peaks from the Gaussian form become more distinct. For instance, shown in Fig. 11 is a diffraction peak measured on a single crystal whose profile includes negative dips on both sides of the peak and for which it is difficult to find an analytical function. Accordingly, for analysis of RTOF spectra by the Rietveld method, a special-purpose package MRIA was developed [37], which provides the possibility of specifying a two-sign model for description of peak profile, with peak set numerically. For a model, as a rule, a single intense peak is selected from a pattern being processed or a pattern measured on the standard sample. Processing of the pattern from the standard polycrystals (Al_2O_3, NAC) showed very good agreement between the structural parameters determined on HRFD and the data in the literature. As an example, Fig. 12 presents a diffraction pattern of NAC processed with MRIA. Comparison of the structural parameters of NAC obtained on HRFD and HRPT showed their identity in relative coordinates at a level of 4×10^{-4}; in interatomic distance, 4×10^{-3} Å; and in thermal factors, 0.2 Å^2.

If necessary, the diffraction spectra measured on HRFD can be processed using the other software packages, such as FullProf, GSAS, or JANA. To do this, one should first perform spectrum normalization and recalculate the dispersions of points. The files with the data and dispersions are converted into the format required by the package. The fact that these programs lack the possibility of specifying a two-sign model leads to some increase in inconsistency factors, but in most cases weakly affects the structural parameters.

5. HRFD RESEARCH PROGRAM

Since the beginning of HRFD operation, a large number of diffraction experiments were conducted. Structures of high-temperature superconductors (HTSC) and hydrogen-containing compounds, various oxides (perovskites, spinels, celites, and others), etc. were investigated. Before commissioning of FSD, a special-purpose diffractometer, HRFD was used to conduct experiments to determine macro- and microstresses in bulky materials and components. An important peculiarity of HRFD is that it provides an easy switching between two different modes of diffractometer operation, of high intensity and of high resolution, without any changes in the scattering geometry. This allows one to conduct experiments in real time with fast (at a level of 1−10 min) recording of neutron diffraction patterns and thus to track changes in struc-
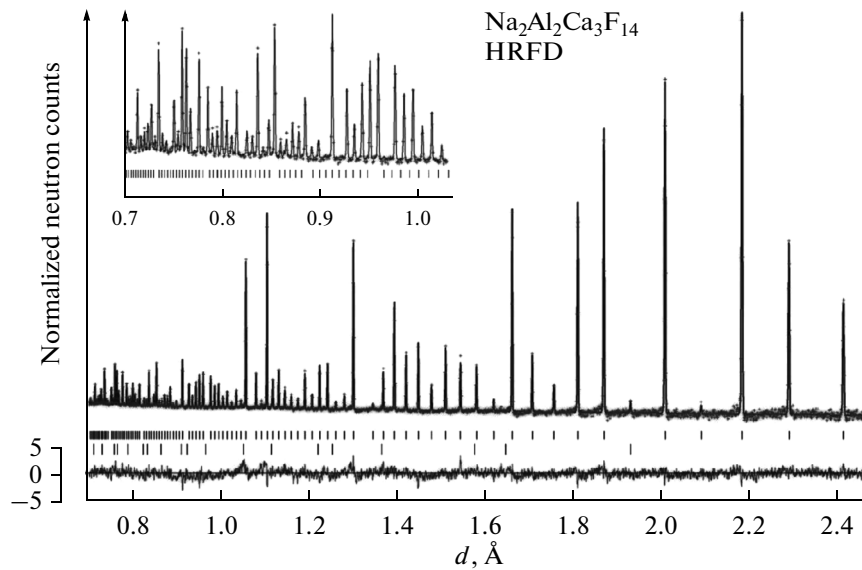
Fig. 12. The NAC diffraction pattern measured at 6000 rpm and processed by the Rietveld method. Shown are the experimental points, the calculated curve, and difference function, which is normalized on the mean-square deviation. The vertical bars indicate the positions of the peaks of the basic (NAC) and impurity (CaF_2) phases.

ture in the course, for example, of temperature scanning. From time to time, scanning is stopped to measure spectrum with high resolution, which is necessary for precise analysis of the structure. This mode is particularly useful for analysis of a multiphase state.
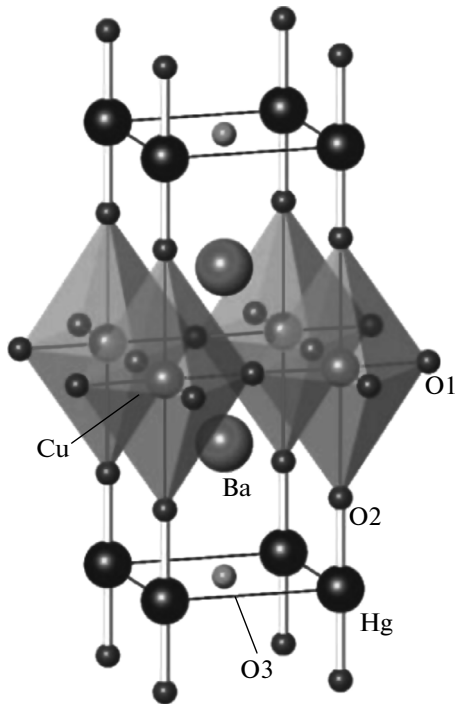
Fig. 13. The image of the $HgBa_2CuO_{4+\delta}$ structure with indicated atoms. The position O3 is filled partially by the value of $\delta \approx 0.1$.

In what follows we analyze in more detail the most typical examples of the research performed on HRFD.

5.1. The Structure of Mercury HTSCs

In a series of studies on mercury-based high-temperature superconductors $HgBa_2Ca_{n-1}Cu_nO_{2n+2+\delta}$ (the major results are reported in papers [38–40] and their survey is contained in [41]), the focus was on the determination of the crystal structure as a function of anion composition (the amount of oxygen or fluorine substituting it) and external pressure. The information concerning the influence of just these two parameters on the structure and properties was expected to be crucial for understanding the formation of superconductivity in mercury cuprates. The necessity of applying neutron diffraction arose from the fact that only it could help to obtain reliable information about anion stoichiometry and configuration of oxygen octahedrons with copper atoms inside. Compositions with $n = 1$ (Hg-1201, oxygen and fluorinated) were mainly examined on HRFD, and structural data of a fundamental nature were obtained for them.

The atomic structure of Hg-1201 ($T_c \approx 97$ K) is shown in Fig. 13. It is relatively simple and has a high symmetry (sp. gr. P4/mmm); accordingly, only some structural parameters are subject to refinement: z coordinates of Ba and O1, thermal factors, and occupancies of individual positions, primarily position O3, which is only partially filled with oxygen. An example of the diffraction pattern of Hg-1201 measured on HRFD and processed by the Rietveld method is given in Fig. 14. Reliable data were needed for the following items: the occupancy factor of the O3 position with
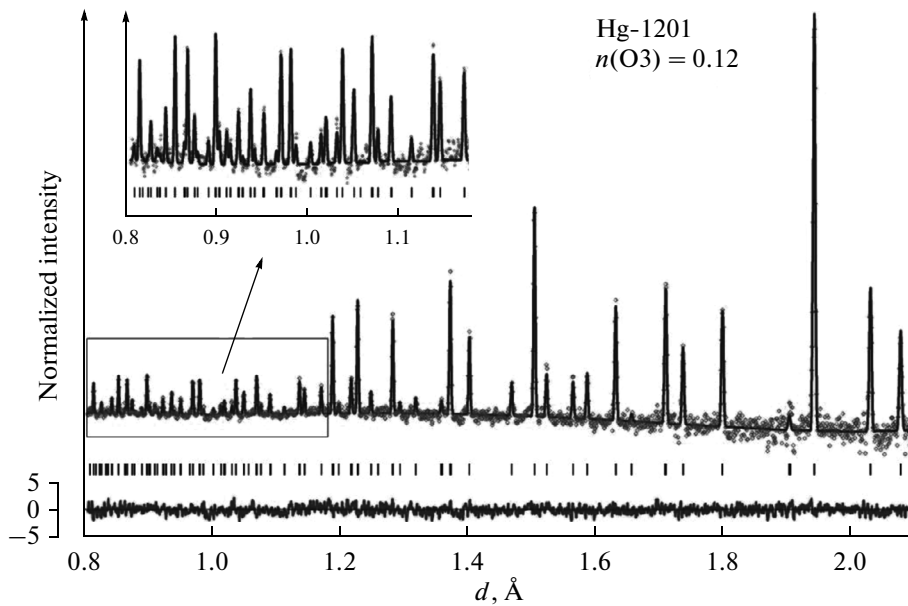
Fig. 14. The diffraction pattern of $HgBa_2CuO_{4.12}$ measured at 4000 rpm and processed by the Rietveld method. The experimental points, calculated curve, and difference function, which is normalized on the mean-square deviation are shown. The vertical bars indicate the calculated positions of the diffraction peaks.

anion (oxygen or fluorine) (δ) and the superconducting transition temperature (T_c) as its function, possible presence of extra oxygen in the plane (ab) of unit cell, the interatomic distances Cu–O2 and Hg–O2 as a function of δ.

The high resolution of HRFD allowed one to observe a large number of distinctly separated diffraction peaks, which in turn made it possible to determine a large number of experimental structural factors needed for constructing the cross sections of scattering density (of Fourier maps). One of such cross sections is shown in Fig. 15, where the atoms of O1, Ba, and O3 are clearly visible and, on the contrary, no additional oxygen atoms, whose presence in the basal plane of the structure was reported in several works, were visible.

The content of extra anion (oxygen or fluorine) for Hg-1201 was determined with an accuracy of 10%, making it possible to surely reproduce the superconducting transition temperature as its function (Fig. 16). Conservation of charge balance and the ionic nature of the formation of carriers in the superconducting plane call for double the amount of univalent fluorine as compared to bivalent oxygen in order to have the same superconducting transition temperatures. The dependences shown in Fig. 16 clearly confirm this idea: the δ values optimal for T_c were 0.12 $\pm$ 0.01 for oxygen and 0.24 $\pm$ 0.02 for fluorinated compositions.

The δ-dependences of apical distances Cu–O2 and Hg–O2 were also interesting (Fig. 17). Unlike the transition temperature, which is related to the charge brought to the basal plane of the structure, these dis-
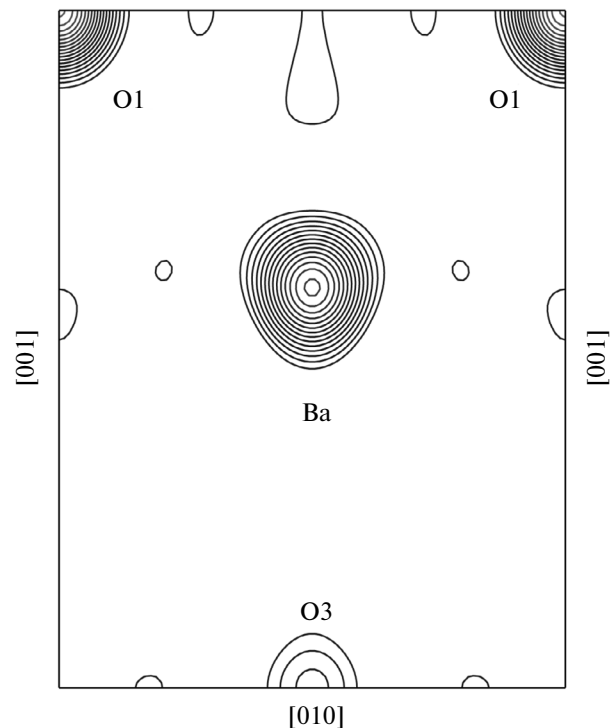

Fig. 15. Fourier map of the scattering density in the unit cell cross section ($x = 0.5$, $0 \le y \le 1$, $0 \le z \le 0.5$) for the sample with $\delta \approx 0.12$, calculated by using experimental F_{hkl}. There are no maxima at the position $y = 0$, $z = 0$.
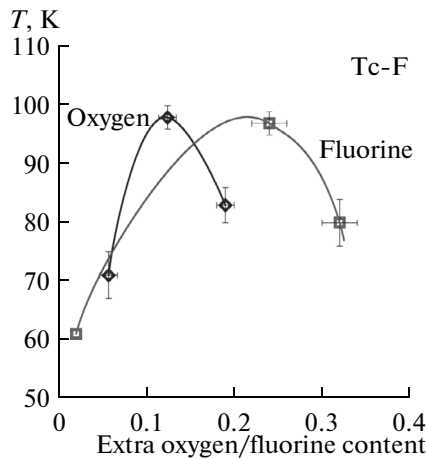
Fig. 16. The temperature of superconducting transition as a function of the amount of doping anion (oxygen or fluorine) for Hg-1201. Characteristic experimental points are only shown for convenience of perception.

Fig. 17. The apical distances of Cu−O2 and Hg−O2 in the Hg-1201 structure as a function of the amount of extra oxygen or fluorine content. The points with anion amount of 0.06, 0.12, and 0.19 correspond to oxygen, the rest (0.24 and 0.32) to fluorine. The compositions with oxygen content $\delta \approx 0.12$ and fluorine content $\delta \approx 0.24$ have the same temperature $T_c \approx 97$ K.

tances change in proportion to the number of anions. On the contrary, the Cu−O distances in the plane (CuO$_2$), just as T_c, are defined by the charge state of the system.

From the point of view of method development it was important to demonstrate the Fourier diffractometry potentials for determining the occupancy factors with accuracy at a level of 0.01 and interatomic distances at a level of 0.003 Å. These values turned out to be almost identical to the results obtained on high-resolution λ_0 diffractometers 3T2 (LLB, Saclay) and D2B (ILL, Grenoble), which were used to make similar investigations (Table 2 from paper [41]).

5.2. Phase Separation in La$_2$CuO$_{4+x}$

Although HRFD is primarily intended for structural studies of polycrystals, it can also be used to examine single crystals if high resolution in reciprocal space is required. Such a need arose during the study of phase separation in crystals La$_2$CuO$_{4+x}$, $x \approx 0.02-0.04$, which occurs as the temperature decreases on scales of around 10^3 Å [42]. According to available views, on cooling of these crystals a low-temperature diffusion of extra oxygen occurs with the resulting formation, in the crystal, of oxygen-poor (P1 phase) and oxygen-rich (P2 phase) regions with slightly different parameters of unit cells. In P1 phase an antiferromagnetic order is established at low temperature, while P2 phase becomes superconducting. In diffraction experiments on HRFD it was necessary to obtain direct evidence of phase separation, try to trace its evolution, and estimate the characteristic size of the formed regions.

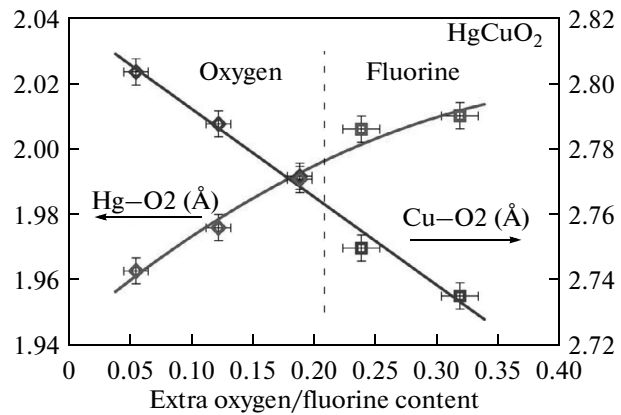A typical diffraction pattern consisting of several orders of reflection in the direction [0k0] of the recip-

rocal crystal lattice is shown in Fig. 18. At $T = 10$ K each of the peaks is split into two components belonging to the phases P1 and P2. A relative difference in the corresponding parameter of the unit cell is about 0.0022 ($b_1 = 13.1203$ Å, $b_2 = 13.1491$ Å); however, the splitting of the peaks is clearly visible. Analysis of the evolution of its appearance with decreasing temperature showed that the signs of the phase splitting appear at ≈ 250 K.

The average characteristic dimensions of the coherently scattering regions for both phases were determined based on the relation (7), from which it follows that if the contribution of the resolution function is quadratically subtracted from the full width of the peak, then the quantity $(\Delta W/d)^2$ must be proportional to $(d/L)^2$, where L is the size of domains in a given direction. This kind of dependences for the directions [0k0] and [00l] are shown in Fig. 19. Based on the slope of the obtained straight lines one can estimate L, which proved to be around 1000 and 1500 Å in the directions [0k0] and [00l], respectively; i.e., separation develops at a mesoscale level.

The series of studies on separation in single crystals La$_2$CuO$_{4+x}$ is also interesting due an efficient combined analysis of data obtained using the neutron diffractometer and the μSR spectroscopy method [43]. Unlike diffraction, the μSR method allows independent tracing of evolution with the temperature of ordered magnetic moment value and the fraction of magnetically ordered phase within the crystal. The revealed correlation between the diffraction and μSR data suggested the occurrence, in La$_2$CuO$_{4+x}$ ($x \leq$ 0.04) crystals, of microscopic phase separation as well, which is stimulated by superconducting transition.

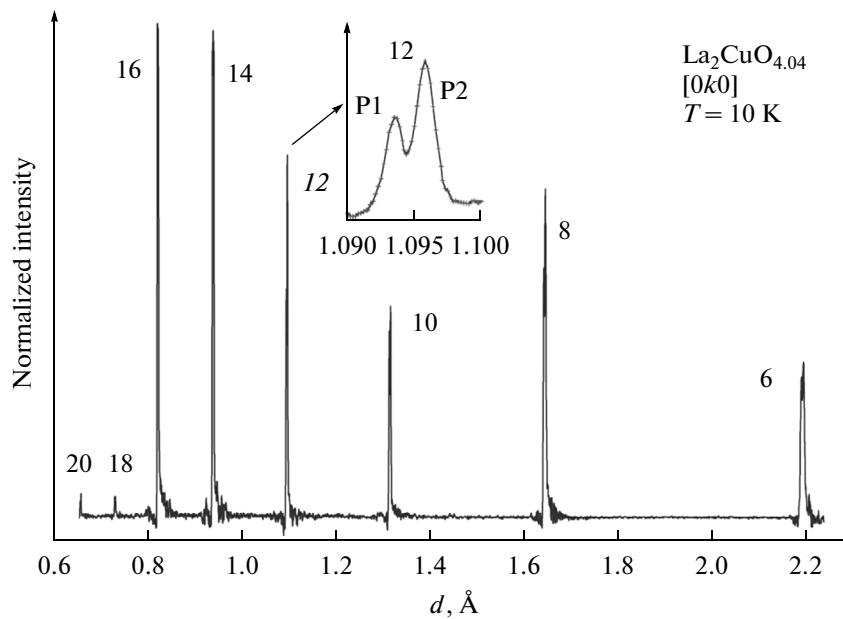**Fig. 18.** The orders of reflection (the numbers next to the peaks) from the plane (010) of the single crystal $La_2CuO_{4.04}$, measured on HRFD at 10 K and maximum chopper velocity 8000 rpm. Each of the peaks is split into two components (shown in the insert for the 12th order), corresponding to two crystalline phases (P1 and P2) with slightly different values of unit cell parameters.

The experiments with La_2CuO_{4+x} have demonstrated the flexibility of the HRFD configuration and showed the importance of the weak dependence of the resolution function on d_{hkl}. It is the latter fact that has allowed one to observe, with confidence, a broadening in several orders of reflection from crystallographic planes and to surely recognize the contribution of the size effect.

5.3. Mesoscopic Phase Separation in $(La_{1-y}Pr_y)_{0.7}Ca_{0.3}MnO_3$

Interest in doped manganese oxides like $La_{1-x}Ca_xMnO_3$, $0 \le x \le 1$ arose in the mid-1990s, after the colossal magnetoresistance (CMR) effect was rediscovered in them—a severe decrease in the electrical resistance of a material by applying an external magnetic field. This effect is due to a phase transition from a dielectric to metallic state, whose temperature (usually in the range of 100 to 200 K) can be shifted by imposing a magnetic field. Compositions with the CMR effect (relative change of resistance) reaching 10^4 and more were found among perovskite manganites. The potential technological applications of such compositions are rather diverse and extremely efficient.

Another intriguing phenomenon observed in manganites was a giant isotope effect discovered by specialists of the NRC "Kurchatov Institute" in 1998 in the composition $(La_{0.24}Pr_{0.75})_{0.7}Ca_{0.3}MnO_3$ [44]. This effect consists in the change of the low-temperature metallic state of this compound to a dielectric one, with isotope ^{18}O in place of ^{16}O.

In a series of studies performed on HRFD, as well as on the neutron diffractometers DMC and HRPT at PSI (Switzerland) (for their brief review, see [45]), it was found for certain that the giant isotope effect and many other specific properties of the perovskite manganites are associated with the occurrence of phase separation in them at low temperatures in a region of mesoscopic ($\sim10^3$ Å) size with different types of magnetic ordering. Here we consider only some results of
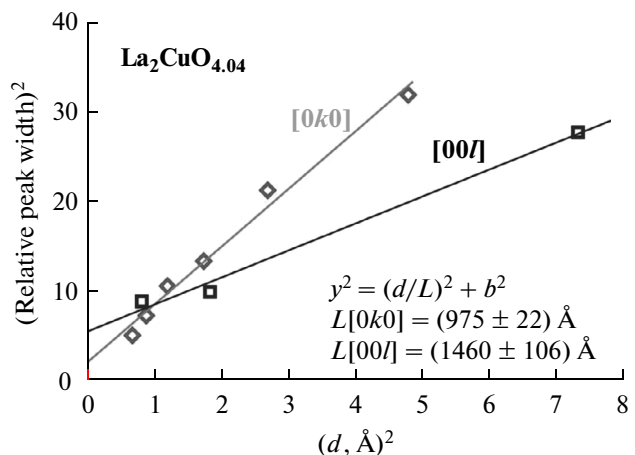

Fig. 19. Contributions to the width of the diffraction peaks connected with the size effect in the (0k0) and (00l) directions. The slope of the straight lines is determined by the characteristic size in a given direction and is about 1000 Å in the direction (0k0) and about 1500 Å in the direction (00l).
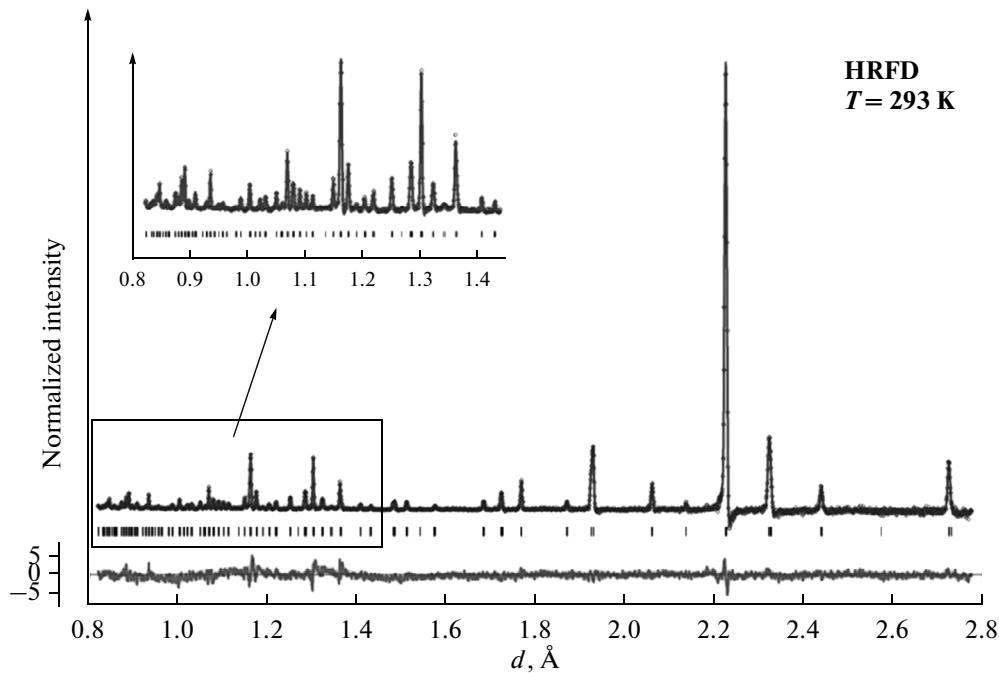
Fig. 20. The diffraction pattern of $(La_{0.25}Pr_{0.75})_{0.7}Ca_{0.3}Mn_{18}O_3$ measured on HRFD and processed by the Rietveld method. The experimental points, calculated curve, and difference curve, which is normalized on the mean-square deviation are displayed. The vertical bars indicate the calculated positions of diffraction peaks.

paper [46], which reports on the analysis of the evolution of the atomic structure of $(La_{1-y}Pr_y)_{0.7}Ca_{0.3}MnO_3$, $0.5 \leq y \leq 1$ as a function of the mean radius of A cation and temperature. For $y = 0.75$ (LPCM-75), structural data were obtained for compositions with the oxygen isotopes ^{16}O and ^{18}O.

Electroconductivity measurements showed that, with decreasing temperature, the composition LPCM-75 containing ^{16}O isotope turns into a metallic state at $T \approx 110$ K, while with ^{18}O in place ^{16}O at a level of 75% and more the composition remains in a dielectric state down to helium temperatures. From the diffraction data obtained on DMC it followed that LPCM-75−^{18}O is an antiferromagnetic at $T \leq 150$ K. AFM phase arises in the composition LPCM-75−^{16}O at the same temperature, but on further cooling there appears FM ordering ($T_c \approx 110$ K), the two-phase state exists at all $T \leq 110$ K; with temperature lower than 10 K the sample's volume parts occupied by the FM and AFM phases are related as 85% to 15%. In subsequent experiments on HRFD, an attempt was made to perceive the causes of this situation.

A typical diffraction pattern of LPCM-75 with ^{18}O isotope is shown in Fig. 20. The quality of the experimental data and their consistency with the proposed model are good enough to get precision structural information. Some points important for an understanding of the situation clearly manifest themselves even in temperature dependences of the parameters of unit cells of LPCM-75 enriched with ^{16}O and ^{18}O

(Fig. 21). First, in the range from 290 K down to LPCM-75−^{16}O transition to the FM phase (110 K), the parameters of unit cells coincide with accuracy better than 0.01%, indicating the full identity of their atomic structures. Second, it is evident that the charge and AFM ordering do not lead to any drastic changes in temperature dependences. Rather, the transition of LPCM-75−^{16}O to the FM phase is accompanied by a sharp reduction of the period along the b axis and a small, yet noticeable, reduction along the c axis.

Subsequent structural analysis confirmed the identity of the structures of both compositions down to the transition of LPCM-75−^{16}O to the FM phase and made it possible to determine the difference between them at low temperatures. It proved to be due to a small (≈ 0.006 Å) difference in the interatomic distance of Mn−O1 (Fig. 22) and a change in the valence angle of Mn−O1−Mn by ≈ 1 deg. Theoretical analysis within the double exchange model supported the association of these structural changes with the change in the phase state of the material. In addition, it became clear that the physical causes of the giant isotope effect are associated with percolation effects—the original AFM matrix is dielectric, but the occurrence of metallic FM clusters in it and the overcoming of the percolation threshold put the material into a state with metallic conductivity.

Largely similar phenomena (including the giant isotope effect) associated with the occurrence of mesoscopic phase separation were subsequently dis-
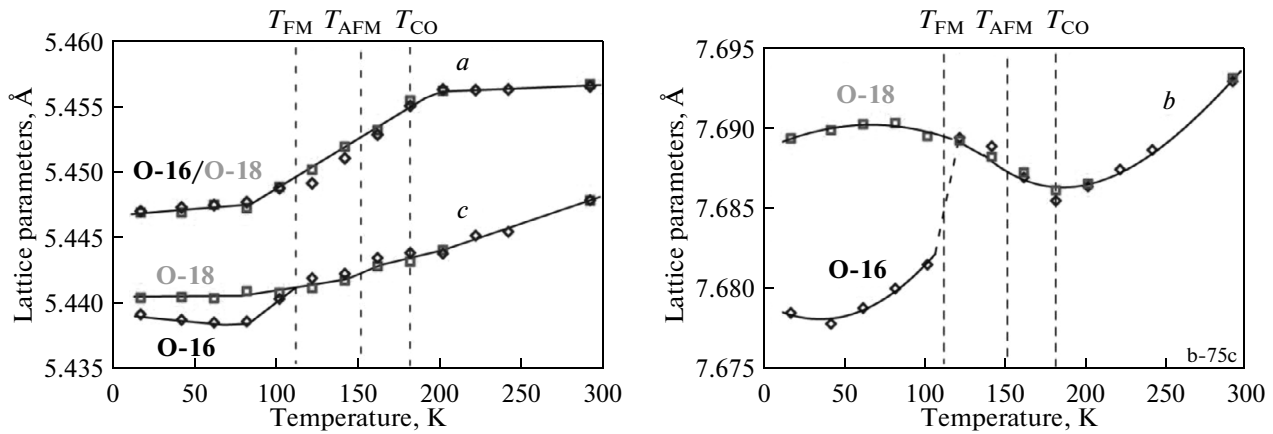
Fig. 21. Temperature dependences of the unit cells parameters of the composition LPCM-75 enriched with isotopes ^{16}O (diamonds) and ^{18}O (squares). Temperatures of transitions (with decreasing temperature) to the charge-ordered state (T_{CO}), AFM phase, (T_{AFM}) and FM phase (T_{FM}, for composition with ^{16}O). The lines are drawn through the experimental points for convenience of perception. The sizes of the symbols are greater than the errors of the data points.
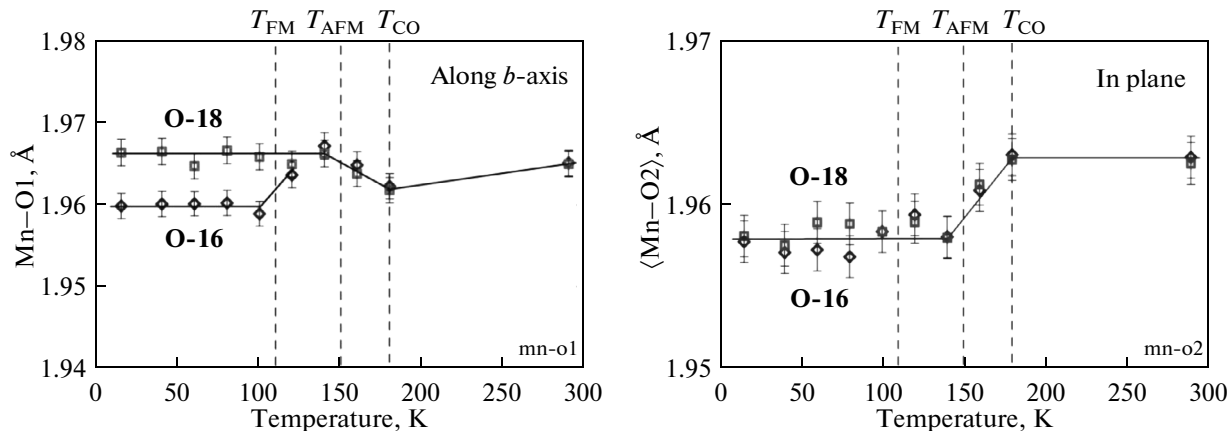

Fig. 22. The same as in Fig. 21 but for the average distance Mn−O2 (right) and apical distance (along b axis) Mn−O1 (left).

covered in strontium-based compositions: $Re_{0.5}Sr_{0.5}MnO_3$ (Re = Sm, Nd, Tb) [47].

In investigations of LPCM and other CMR compounds with the giant isotope effect, the accuracy of interatomic distance determination in powder experiments was brought to 0.001−0.002 Å, which corresponds to the level achieved in the structural studies with single crystals. It is this accuracy that proved to be necessary for a reliable determination of the influence of isotope substitution on the atomic structure of a crystal.

5.4. Microstructural Effects in Oxides

The physical properties of bulky (and, to an even greater extent, nanostructured) crystalline materials largely depend on their microstructure, i.e., on the grain size, number and type of defects, residual mechanical stresses, presence of impurity phases,

topology of grain boundaries, crystallographic texture, etc. High-resolution neutron diffraction is one of the most informative methods used for studying the microstructure of crystalline materials because it has a number of significant advantages over the other known methods.

At present there are several approaches to extraction of microstructural information from measured diffraction pattern. One of the most promising methods is to describe diffraction profiles directly in terms of the physical models of microstructural and lattice defects present in a material under study [48]. However, the Williamson−Hall method, with its representation for TOF diffractometer case in the form of (7), retains its validity for the primary estimation of the microstructural parameters of a material being studied. The usual procedure in this case is the following. First comes pattern processing by the Rietveld method, which can be helpful in obtaining precise
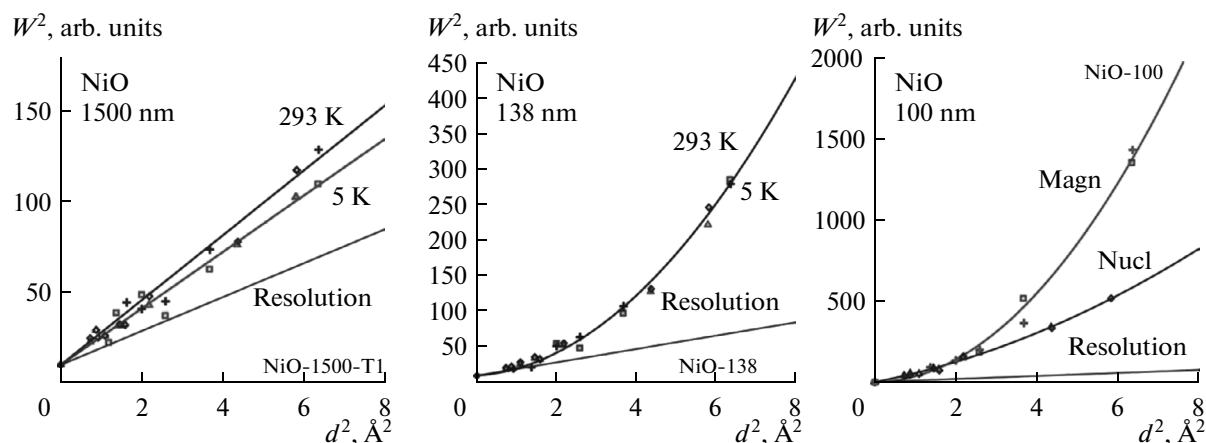
Fig. 23. The dependences $W^2(d^2)$ for the widths of diffraction peaks in NiO powders with mean sizes of crystallites $\langle D \rangle = 1500$ (left), 138 (center), and 100 nm (right) and for the resolution function (lower straight line). The experimental points are shown for the crystalline and magnetic peaks and for two temperatures: 293 and 5 K. The dependences are linear for $\langle D \rangle = 1500$ nm and parabolic for $\langle D \rangle = 138$ and 100 nm. The sizes of the coherent-scattering domains for the nuclear and magnetic structures coincide for $\langle D \rangle = 1500$ and 138 nm and differ greatly for $\langle D \rangle = 100$ nm ($L_{nuc}/L_{mag} \approx 2.5$).

parameters of the unit cell. Then the widths of individual diffraction peaks are determined and in case of strong overlapping of peaks their positions are fixed in accordance with the obtained values of the cell parameters. The found quantities—the full width at half maximum and integral widths—are analyzed using Eq. (7).

A recent example of applying this approach to the data collected on HRFD is paper [49], which presents the results obtained on NiO powders with the mean size of crystallites $\langle D \rangle$ from 13 to 1500 nm. The principal aim was to try to determine how the long-range order of the crystal and magnetic structure depends on the size of the crystallites.

The diffraction pattern of a sample with $\langle D \rangle = 1500$ nm are shown in Fig. 8. Their peculiar feature is that all crystal and magnetic peaks (G-type AFM structure) are separated, all magnetic peaks are single, some nuclear peaks are single, but there are also strongly overlapping ones due to weak rhombohedral lattice distortions.

Figure 23 shows dependences $W^2(d^2)$ for the widths of nuclear and magnetic peaks in NiO powders with mean crystallite sizes of 1500, 138, and 100 nm measured at temperatures of 293 and 5 K. One can assume that for $\langle D \rangle = 1500$ nm they are linear to a good accuracy (there is no size effect), the slope is only slightly higher than that for the resolution function; i.e., the microstrain level is small and still further decreases slightly with decreasing temperature. In contrast, the dependences are parabolic with good accuracy for $\langle D \rangle = 138$ and 100 nm; i.e., the size effect shows itself, but there is no temperature dependence due to a small contribution to the peaks' widths from microstrains. It is also seen from the figures that the sizes of the coher-

ent scattering regions for the nuclear and magnetic structures coincide for $\langle D \rangle = 1500$ and 138 nm and differ greatly for $\langle D \rangle = 100$ nm ($L_{nuc}/L_{mag} \approx 2.5$). That is, in this case the long-range magnetic order in the surface of the crystallites is appreciably destroyed.

Other illustrations of the microstructural effects are depicted in Fig. 24, where we can see different types of $W^2(d^2)$ dependences with manifestation of only the microstrain effect (for $CaCuMn_6O_{12}$) and the anisotropic size effect (for β-$Ni(OH)_2$). In the latter case the strong difference in widths (anisotropic broadening) for different sets of Miller indices allows one to reconstruct the shape of the coherently scattering regions. Calculations showed that these are disk-shaped, with a diameter of ~350 Å and a height of ~150 Å. Electron microscopy analysis showed that indeed the shape of the particles is discoid, with a diameter and height of ~1500 and ~200 Å, respectively. From comparison with the diffraction data it follows that the structure of the particles has a long-range order only in the center of the disks, while their periphery is amorphized.

The findings of the investigation into the microstructural effects in crystals and the model calculations showed that the resolution of HRFD allows one to reliably determine microstrains in crystallites at a level of $\varepsilon \approx 0.0008$ and more and the mean size of coherently scattering domains at a level of $L_{coh} \approx 350$ nm and less. In addition, anisotropic peak broadening effects are determined with confidence. In these cases the weak dependence of the resolution on d_{hkl} is an important factor, making possible the use of a large number of experimental points for plotting and analysis of the function $W^2(d^2)$.
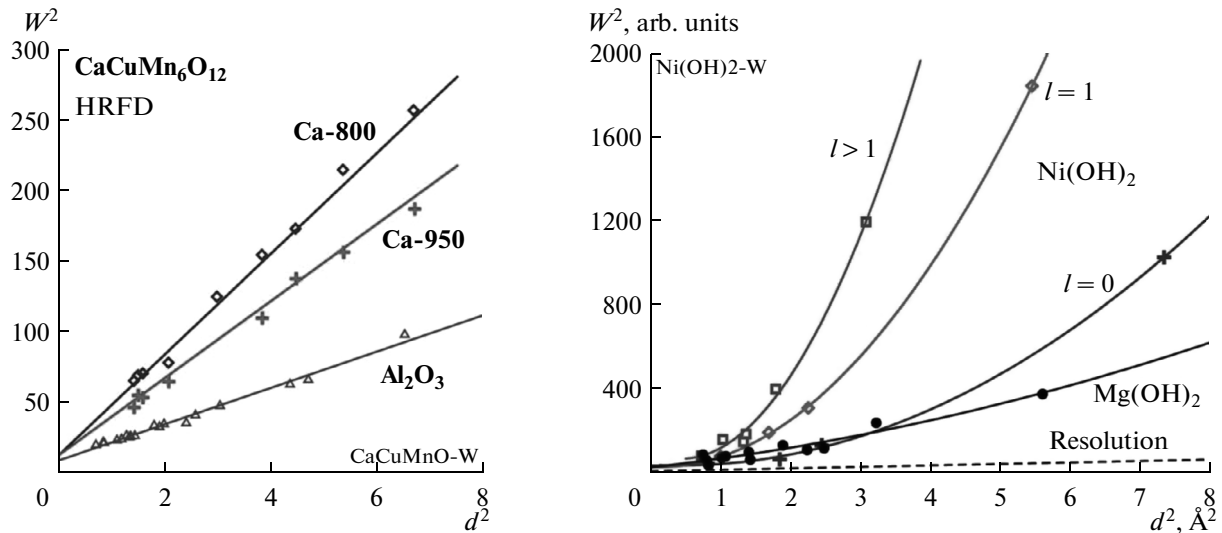
Fig. 24. The dependences $W^2(d^2)$ for the widths of diffraction peaks in the compositions $CaCuMn_6O_{12}$ (left) and β-$Ni(OH)_2$ (for different values of the index *l*) and $Mg(OH)_2$ (for all *hkl*) (right). Dependences for two compositions $CaCuMn_6O_{12}$ prepared at different quenching temperatures (800 and 900°C) and differing in the level of microstrain (with no size effect). For $Mg(OH)_2$ and β-$Ni(OH)_2$ the dependences are parabolic (with size effect), for β-$Ni(OH)_2$ a strong broadening anisotropy is observed.
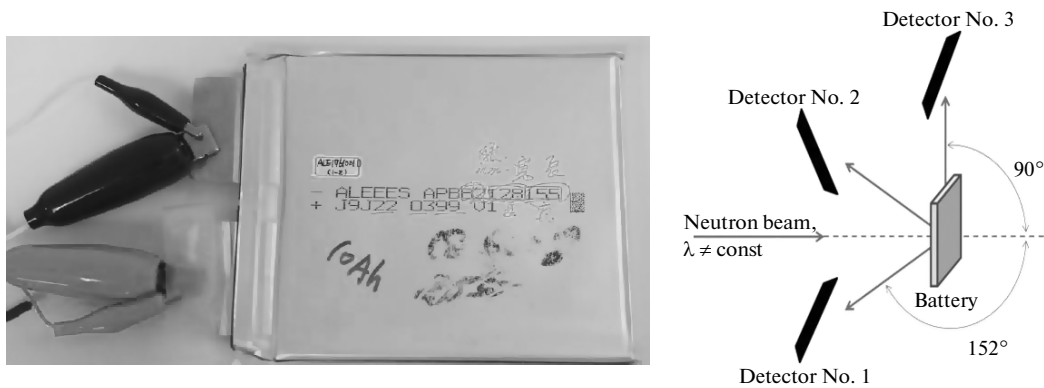

Fig. 25. The external view of a Li-ion battery (linear dimensions $8.2 \times 128 \times 155$ mm) of capacity 10 A h (left) with current outputs and the diagram of its location relative to the neutron detectors on HRFD (right). The other battery (of capacity ~ 2 A h, with no vanadium doping) studied on HRFD had a similar size.

5.5. In-Situ Real-Time Investigations of Li batteries

The crystallographic methods are widely applied to clarify the structural peculiarities of the cathode materials used in electrochemical sources of current, including Li batteries, and neutron diffraction has become one of them. This is facilitated by such features as the sensitivity to light elements, the ability to distinguish between elements with similar atomic numbers, and high penetrability.

On HRFD, a study [50] was done into charge–discharge processes of two flat batteries (Fig. 25), with pure $LiFePO_4$ (lithium-ferrophosphate, LFP, Battery No. 1, capacity ~2 A h) used as positive electrode (cathode) in one of them and lithium-ferrophosphate doped with vanadium oxide ($LiFePO_4 : V_x$, $x \approx 0.01$, LFPV, battery No. 2, capacity ~10 A h) in the other.

Specially prepared graphite served as anode in both batteries.

An array of diffraction data (in 2D representation) obtained in the low-resolution mode (without correlation analysis) in the course of three charge—discharge cycles (each cycle lasted about 20 h) is shown in Fig. 26. Astronomical time (in hours) is plotted as ordinates, while interplanar distances (in Å) are plotted as abscissas. Above are the positions of diffraction peaks for the three main structural phases of the LFP battery, being uniquely characterized by their set. The most intense lines in the range of 3.2 to 3.7 Å are due to the graphite electrode; in the range of 2.2—3.2 Å one can see several intense peaks from $LiFePO_4/FePO_4$ phases. The diffraction data were collected in the high-resolution mode at regular intervals, allowing a
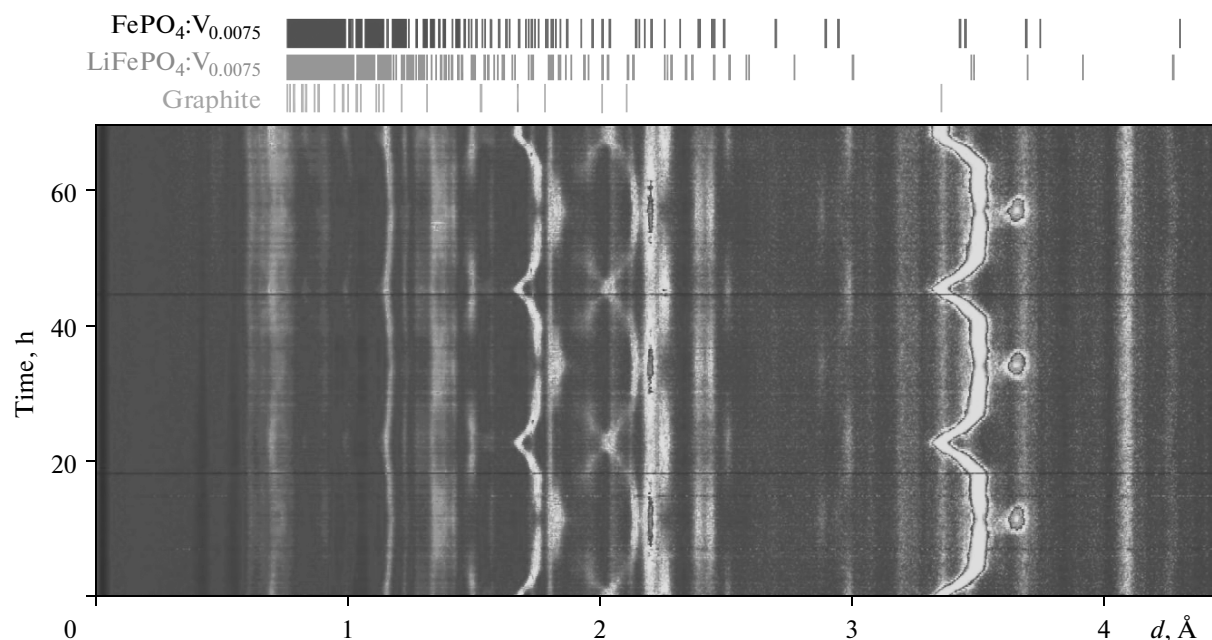
Fig. 26. The evolution of the diffraction pattern from LFP battery with vanadium doping obtained during three complete charging-discharging cycles. Along the *x* axis is interplanar spacing in Å, along the *y* axis is time in hours. One charging-discharging cycle takes about 20 hours. The vertical dashes at the top indicate the positions of diffraction peaks of the three basic structural phases in their initial state.
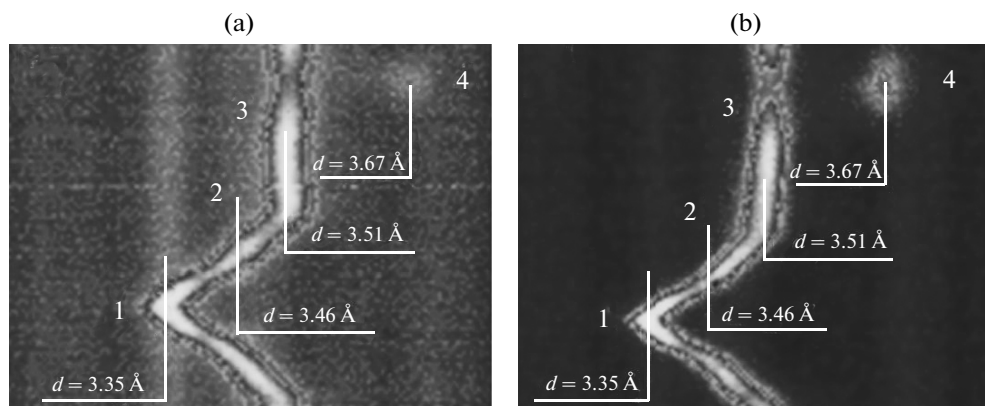

Fig. 27. The zoomed region of diffraction 2D pattern characterizing the structural processes in the LFP battery anode during the charging process. Indicated are the initial state of the anode − graphite without lithium (1, $d = 3.35$ Å) and sequentially forming phases LiC_{27} (2, $d = 3.46$ Å), LiC_{18}, LiC_{12} (3, $d = 3.51$ Å) and LiC_6 (4, $d = 3.67$ Å) for battery No.1 (left) and No. 2 (right).

reliable determination of the qualitative characteristics of the resulting structural phases. Thus, at 50% battery charge the diffraction pattern contained peaks corresponding to six structural phases, and the necessary data could only be obtained at a high resolution of the diffractometer.

Analysis of the diffraction peaks pertaining to graphite made it possible to trace in detail the staging of the process of embedding lithium in graphite with subsequent formation of several LiC_n phases (Fig. 27). First one can observe a gradual increase in the distance between the carbon layers into which lithium is implanted. In the next stage the period increases insignificantly, which corresponds to the implantation of lithium ions into the basal planes of the graphite structure. The formation of the final LiC_6 phase during charging is well detected by the abrupt appearance of a diffraction peak at $d \approx 3.67$ Å. In a fully charged state the LiC_6 phase occupies around 50% of the initial volume of the graphite electrode, the rest being not fully occupied by lithium saturated phases (mainly LiC_{12}). In the LFPV battery, a portion of the anode material greater by 10% than that in a battery with conventional $LiFePO_4$ turns into the LiC_6 state.
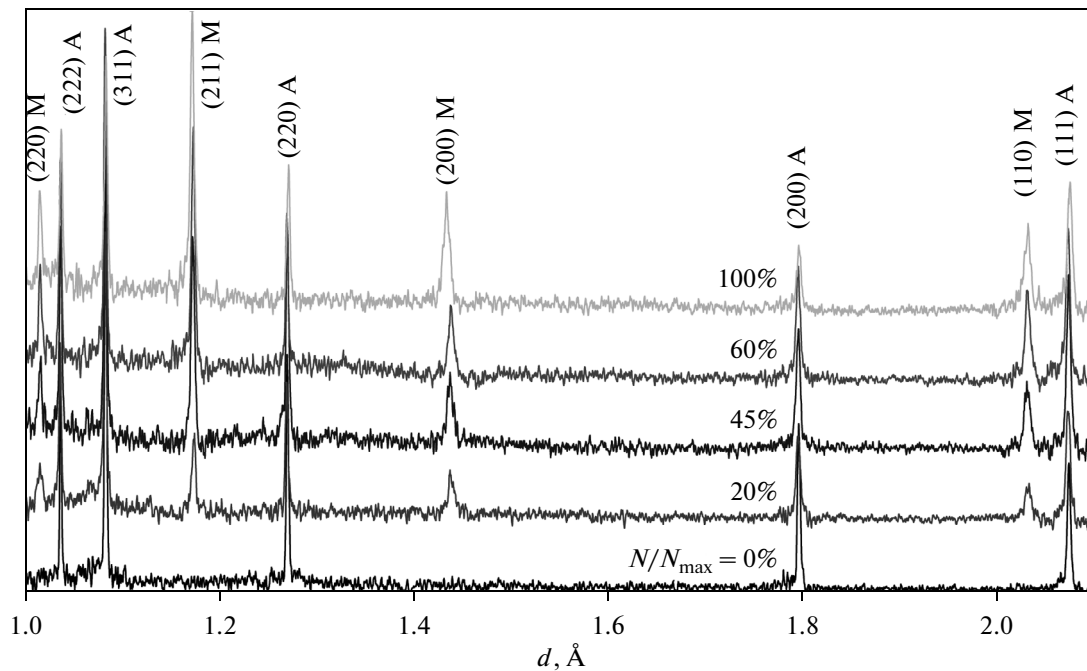
Fig. 28. The evolution of the austenite steel diffraction pattern as a function of the degree of the material fatigue, N/N_{max}, N is the number of tension−compression cycles with maximum deformation ±0.6% and frequency 0.1 Hz, N_{max} = 1020 is the beginning of fatigue failure. The Miller indices of the initial austenite phase (A) and new martensite phase (M) are indicated. The martensite phase emerges even at N/N_{max} = 0.2.

Thus, the neutron diffraction experiments with LFP and LFPV batteries carried out on HRFD have enabled a real-time examination of the transition processes taking place in their electrodes during the charge−discharge cycles. The data obtained have provided a reliable identification of the emerging structural phases and, in principle, a qualitative analysis of the kinetics of phase transformations in the anode and cathode. An important feature of these experiments was the possibility of switching between two different (high-intensity and high-resolution) modes of the diffractometer operation with no change in the scattering geometry.

5.6. Solution of Materials Science Problems

Diffraction of thermal neutrons is one of the most informative and nondestructive methods when solving many applied engineering and materials science problems, and it has a number of significant advantages over the other techniques. The main advantages of this method are deep scanning of the material under study (up to 2 cm for steel), high spatial resolution (up to 1 mm in any dimension), simultaneous measurement of the average lattice deformation for a measured volume and microstrain within the grains, determination of the crystallographic anisotropy of deformations, determination of stress distributions for each component of the multiphase material separately, and the

possibility of investigating both magnetic and nonmagnetic materials.

In view of great potential of this area of research, soon after the commissioning, work was started on HRFD toward the construction of extra equipment and the first experiments were conducted to study internal mechanical stresses in industrial components and promising structural materials. Below are two examples of such studies done on HRFD.

Fatigue properties of austenitic steel X6CrNiTi1810. Austenitic steels enjoy wide commercial application because of their high strength and corrosion resistance. For high-strength material production, of special interest are such mechanical properties of austenitic steels as creep, formation of new phases, mechanical and thermal fatigue, and peculiarities of fatigue failure under cyclic loads. HRFD was used to study the elastic properties of the austenitic steel X6CrNiTi1810 under uniaxial external load and residual internal stresses due to cyclic fatigue of the material [51].

When studying the fatigue properties, a series of cylindrical samples were subject to a various number of tension−compression cycles with a maximum deformation of ±0.6% and a frequency of 0.1 Hz. The experimentally determined number of cycles corresponding to the total material fatigue upon appearance of cracks and initiation of fatigue failure turned out to be equal to $N_{max} \approx 1020$. For samples with different degrees of material fatigue N/N_{max}, neutron diffraction experiments were conducted with a view of deter-
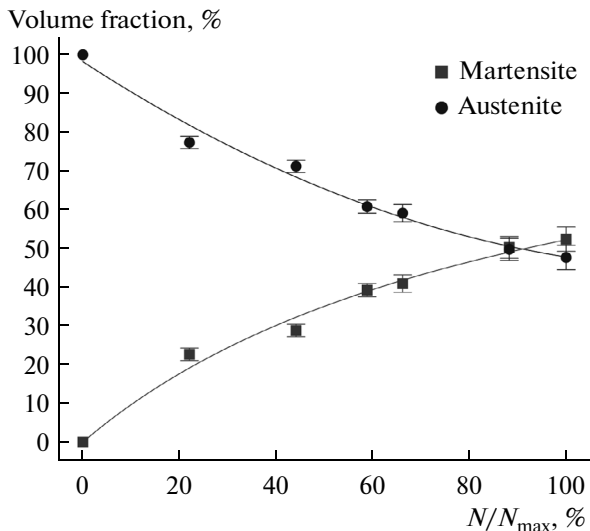
Volume fraction, %

Fig. 29. The volume fractions of the austenite and martensite phases as a function of the degree of the material fatigue, obtained during the processing of diffraction spectra by the Rietveld method.

mining their phase state and the magnitude of residual mechanical stresses.

The diffraction peaks from the initial austenitic phase corresponded to a face-centered cubic (FCC) structure (sp. gr. $Fm3m$). The appearance of diffraction peaks characteristic of a martensitic body-centered cubic (BCC) structure (sp. gr. $Im3m$) was observed (Fig. 28) in the patterns a with an increasing degree of material fatigue. Its tetragonal distortion was not observed, which is due to low content of carbon (0.04%) in this type of steel. The pattern processing by the Rietveld method allowed a quantitative estimate of the volume content for each phase, depending on N/N_{max} (Fig. 29). Before the fatigue failure, the volume fractions of the austenitic and martensitic phases become equal, which is responsible for the occurrence of cracks due to strong stress at the phase boundaries.

Ceramic matrix composites Al_2O_3/Al. The development of technology for new materials has led to a new method of producing composite materials in which a metal is infiltrated into a porous ceramic matrix under gas pressure. Brittle ceramic materials are reinforced by the inclusion of an elastic phase, usually by a metal, which enables one to improve the mechanical characteristics of such composites. The metal in this case is usually infiltrated into a matrix at temperatures slightly higher than the metal melting point. The most typical materials of this kind are composites Al_2O_3/Al, with metal Al phase infiltrated into a porous ceramic α-Al_2O_3 matrix. Because of the significant difference in the coefficients of thermal expansion ($\alpha = 8.3 \times 10^{-6} \deg C^{-1}$ for Al_2O_3, $\alpha = 22.5 \times 10^{-6} \deg C^{-1}$ for Al), the metal phase, when cooled, experiences greater compression that the ceramic phase does. That is why

one can expect that in metal there will be tensile residual stresses, while in ceramics there will be compressive ones.

Two series of composites Al_2O_3/Al with an average size of metallic inclusions of 0.1 and 1 μm were investigated on HRFD [52]. In each of these series, the matrix porosity and, accordingly, the volume fraction of Al were 15%, 25%, and 35%. The diffraction pattern of all the samples contained well resolved peaks of both phases (Fig. 30). Changes in the lattice parameters in relation to the content and average size of metal contamination, as well as respective residual deformations averaged over all available reflexes (*hkl*), were determined by the Rietveld method for the matrix of Al_2O_3. In the Al_2O_3 phase, there was no preferred orientation of crystallites, whereas there was a strong texture in the metal phase, and therefore the strains were calculated based on the results of processing of individual diffraction peaks.

In the composites being studied, the Al_2O_3 phase turns out to be under the action of compressive stress, while the metal phase is under tensile stress (Fig. 31). The stress in the Al phase decreases with increasing content average size of the metal inclusions. The behavior of stress in the matrix is more complicated and strongly dependent on the microstructure of the composite.

The high resolution of HRFD also allowed for estimating the microstress level in the material on the basis of a precision analysis of diffraction peaks broadening. As expected, the residual microstress level in both phases of the composite increases almost linearly with increasing content of the metal phase of Al (Fig. 31). The residual microstress level in both phases for a fine-grained structure (0.1 μm) is on average higher than for a coarse-grained one (1 μm).

6. TECHNICAL PROBLEMS OF FOURIER DIFFRACTOMETER AND THEIR SOLUTIONS

During the operation of HRFD, some technical problems were revealed, some units were upgraded, and the way to improvements in diffractometer luminosity and resolution were elaborated. One of the most serious problems directly affecting the quality of the obtained information is the complex shape of the diffraction peaks (Figs. 4, 11) and its dependence on the adjustment of the diffractometer parameters. From the viewpoint of further development, of most importance is to improve the luminosity of HRFD, which in turn is primarily associated with the increase in the solid angle of the detection system. Finally, the quality of correlation analysis of events being measured largely depends on the data acquisition system and on its adjustability for a specific mode of operation.
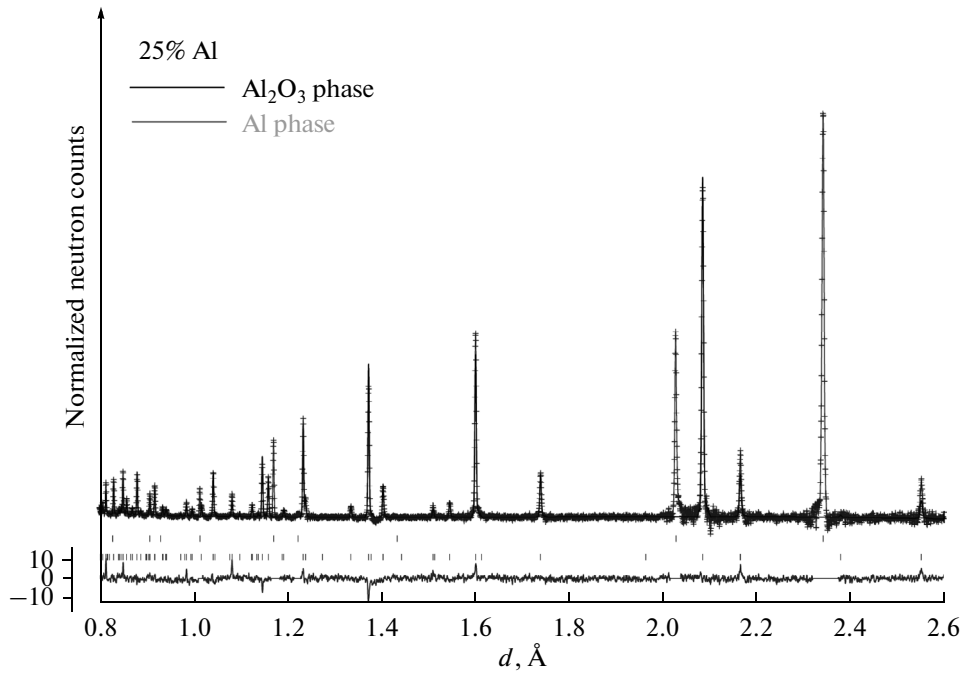
Fig. 30. A part of the neutron diffraction pattern of the composite Al_2O_3/Al with a volume fraction of metal phase of Al equal 25% and average size of metallic inclusions ~1 μm. Shown are the experimental data points, the profile curve calculated by the Rietveld method, and the difference curve normalized to root-mean-square deviations of the experimental points. From top to bottom dashes show the calculated positions of the diffraction peaks for the phases Al and α-Al_2O_3, respectively. Reflections of the textured Al phase were not included in diffraction pattern profile fit.

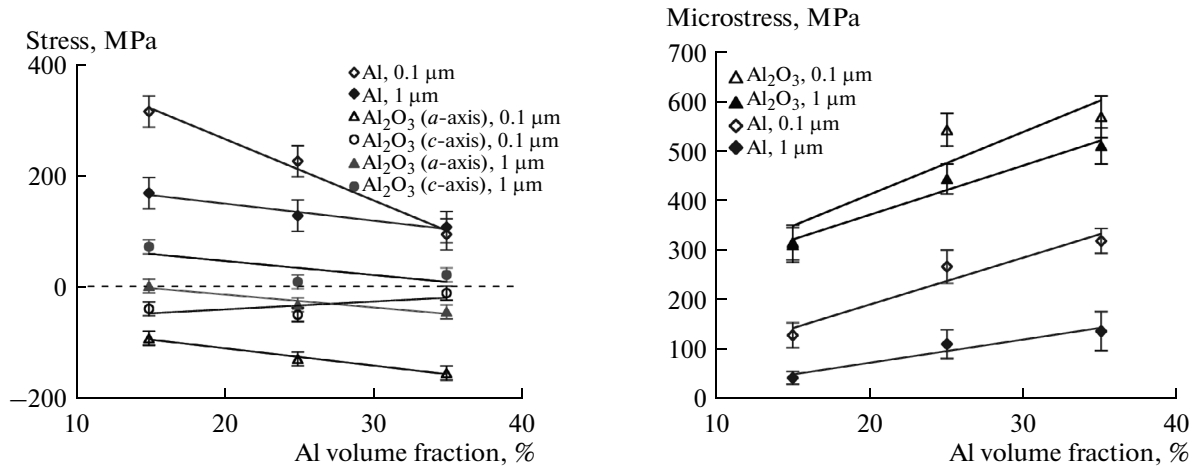**Fig. 31.** Residual stress (left) and microstress (right) in the composite Al_2O_3/Al with fine- and coarse-grained microstructure as a function of Al volume fraction.

6.1. Resolution Preserving Increase of the Main Detector Solid Angle

The luminosity of the neutron diffractometer is convenient to be estimated using the parameter

$$I = \Phi_0 S \delta \Omega_D / 4\pi, \qquad (9)$$

where I[n/s] is the neutron counting rate in the detector, Φ_0 [n/cm²/s] is the total neutron flux on a sample, S [cm²] is the effective area of a sample, δ is the scat-

tering power of a sample in 4π steradian, Ω_D [sr] is the detector solid angle. For HRFD backscattering detectors, with Fourier chopper extracted from the beam, $\Phi_0 \approx 1.3 \times 10^7$ n/cm²/s, $S \approx 3$ cm², $\Omega_D = 0.16$ sr, i.e., for δ = 0.1 we get $I \approx 5 \times 10^4$ n/s. This magnitude is enough for relatively fast data acquisition in the low-resolution mode, but change-over to the high-resolution mode leads to about tenfold reduced luminosity, which is no longer suited to modern requirements.
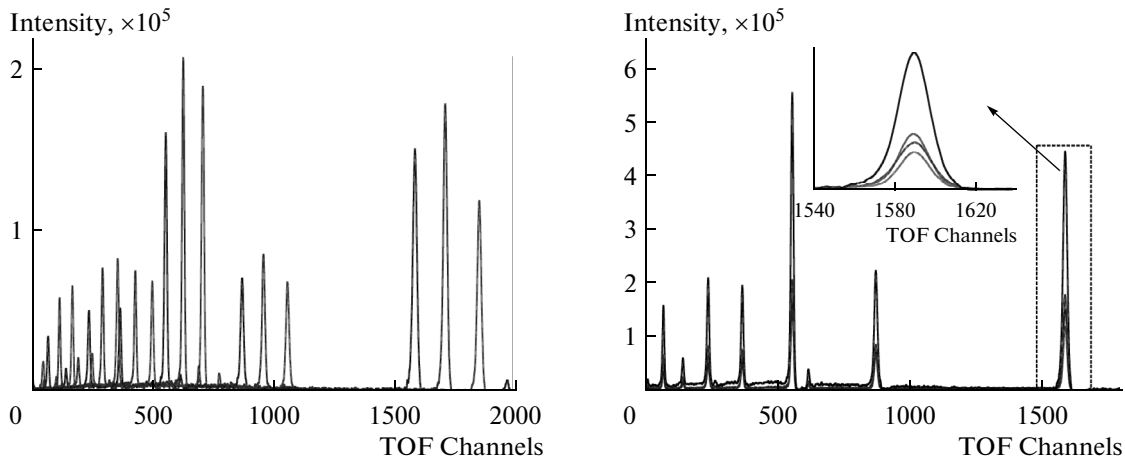
Fig. 32. Diffraction patterns measured by three elements of the ASTRA detector (left). The same patterns after adjustment to a single time-of-flight scale transform into the final summarized pattern (right).

Luminosity can be improved by increasing the neutron flux and the detector solid angle, but the primary reserve is the increase of Ω_D. The HRFD detectors are designed so that their entire surface satisfies the condition of geometrical focusing. This condition was necessary in the early 1990s because it allowed signals from the whole area of the detector to be processed by only one electronic unit of correlation analysis. Such a design, however, led to an almost grazing incidence of the neutrons scattered by the sample onto the surface of the detector, and, despite a relatively large area ($\sim$0.5 m^2), the solid angle of one backscattering detector is accordingly only 0.08 sr.

In addition to the insufficient solid angle, the HRFD detectors have another drawback—too high sensitivity to γ background, since for a detecting element they use Li-glass based scintillators. Both problems can be solved by using ZnS(Ag)-based scintillators and applying a combined electron–geometric focusing [53]. One of the possible versions of a new backscattering detector is given in paper [32]. The detector has a ring structure and comprises $\sim$200 separate elements the light from which is collected with wavelength-shifting fibers. The total area of the detector elements is about 13.5 m^2, which provides a solid angle of about 1.8 steradian. Signals from each of the detector elements are registered independently and each element's configuration satisfies the time focusing condition. The geometric contribution to the resolution function depends on the distance of the detecting element from the neutron beam (from the ring radius) and varies from 0.0004 to 0.0009. The subsequent summation of the diffraction pattern measured by separate elements is performed by a computer with due regard to a specific situation. For instance, it can be done over the whole area of the detector or its separate rings.

The combined focusing enables one to significantly increase the detector solid angle and, at the same time, maintain a reasonable number of independent data acquisition channels. A largely similar idea has been realized on the FSD facility in the form of a multielement detector ASTRA, which in full version consists of 56 independent acquisition channels [54, 55]. The patterns measured by separate elements of the detector and reduced to a single time-of-flight scale are shown in Fig. 32.

6.2. List-Mode Data Acquisition

The electronics to acquire experimental data on HRFD were developed according to the emerging new opportunities. The first version of the correlation electronics was realized on parallel RTOF correlators specially designed at the VTT Technical Research Center of Finland, Espoo, and used earlier on the mini-SFINKS Fourier diffractometer [19, 56]. The next stage of development of the correlation electronics was VME-standard correlators' apparatus based on programmable digital signal processors [57]. At present, both Fourier diffractometers at the IBR-2 reactor are being switched to a new data acquisition system in list mode (list-mode analyzer) [58].

Unlike earlier analyzers, this system registers single events rather than a histogram (diffraction pattern); to do this, the absolute time of an event and its features, written as a word to the computer disk, are detected with high accuracy. The features of an event include, for example, the number of activated detector, the state of a pick-up signal, the state of the reactor, etc. Four-byte long words are sufficient for HRFD. Among the advantages of this data recording method is the possibility of data acquisition from a large number of independent detector elements and the ability to
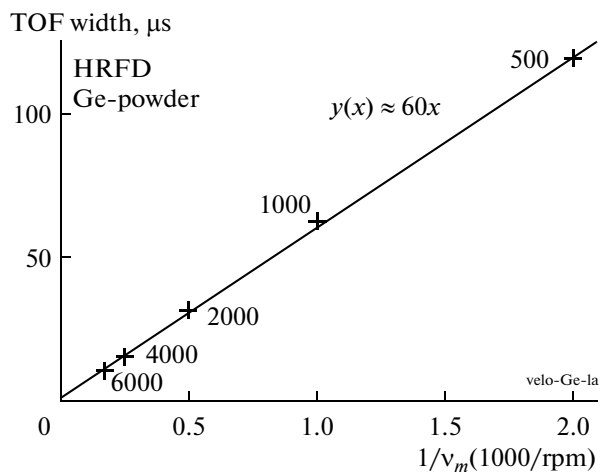
Fig. 33. The effective pulse width as a function of the maximum velocity of the Fourier chopper. The experimental points are obtained for V_m from 500 to 6000 rpm (the velocity is shown next to the data points). The dependence obtained is well approximated by the linear function $y = 60x$.

store the experimental data in their original form. The latter allows applications of the software for multiple data processing with insertion of necessary corrections into the processing algorithm.

6.3. Improvement of the HRFD Resolution

The resolution of HRFD is mainly dependent on the maximum rotation frequency of the Fourier chopper ν_{max}. From Eq. (3) it follows that the time component width of the resolution function is $W_c \approx 1/N \cdot \nu_{max}$, where N is the number of slits on the chopper. Measuring the width of the diffraction peaks as a function of d_{hkl} and ν_{max}, one can determine W_c for different ν_{max} and check how well they fit the prediction. The experimental points and the calculated line are shown in Fig. 33, which demonstrates that the fit is good and one can expect further decrease in W_c with increasing ν_{max}. For $\nu_{max} = 11.000$ rpm W_c is 6.2 μ_s, and with increasing flight path between the Fourier chopper and the detector (up to 30 m) the time contribution to the resolution function W_c/d becomes close to 0.0002 when $d = 2$ Å. The geometric contribution can be made approximately the same, and hence $\Delta d/d \approx 0.0003$ at $d = 2$ Å, which is close to the resolution of the powder diffractometers at synchrotron radiation sources.

Besides, somewhat better resolution of HRFD can be expected after changing to list-mode data recording and multielement detection system. One of the factors is a better alignment of diffraction peaks positions measured by separate elements of the detector than is possible with geometric alignment. An additional factor is the possibility of more accurate approximation of the saw-tooth function of Fourier chopper transmission by introducing a multilevel pick-up signal.

7. CONCLUSIONS

Featuring all the advantages of the conventional TOF diffractometer, the Fourier diffractometer, as compared to the latter, allows for achieving an extremely high resolution at relatively short flight path, which contributes to the increase of the neutron flux on a sample and to the reduction of the facility costs. Of importance is the weak dependence of the resolution function on the interplanar spacing over rather a wide range. Very unpleasant for conventional TOF spectrometers, the problem of the source pulse overlapping does not exist for the Fourier diffractometer. To the best advantage it can be used at a neutron source with long (>300 μs) pulse.

Technically, the Fourier diffractometer differs from the conventional TOF diffractometer by the presence of the Fourier chopper with a revolution control system, which is in principle a fairly simple device. An essential simplifying circumstance is that there is no need for synchronization of the Fourier chopper rotation with the source power pulses. The most serious technical problem that deserves special attention is the complex shape of diffraction peaks. Accordingly, special methods are required for pattern processing by the Rietveld method. The change-over to the list-mode data acquisition will allow one to overcome this problem to a great extent.

HRFD, in operation at the IBR-2 reactor since 1994, has shown its high performance in a variety of structural experiments with poly- and single crystals and in analysis of the microstructure of crystalline materials. The resolution $\Delta d/d \approx 0.0009$ was practically achieved for a chopper rotation frequency of 6×10^3 rpm and the level $\Delta d/d = 0.0003$ is theoretically possible with increasing maximum frequency of chopper revolutions and lengthening of flight path.

Equipping HRFD with the new multielement detection system and changing to list-mode acquisition of experimental data will make it among the world's best powder neutron diffractometers in basic parameters, luminosity and resolution.

ACKNOWLEDGMENTS

ment, the construction of HRFD was significantly contributed by P. Hiismäki (VTT, Espoo, Finland) with colleagues, V. A. Trunov's group (PNPI, Gatchina) and V. L. Aksenov (JINR, Dubna). V. A. Kudryashev and A. P. Bulkin took an active and very constructive part in the development of HRFD at the IBR-2 reactor throughout the whole 20-year period.

REFERENCES

1. A. W. Hewat, "Design for a conventional high resolution neutron powder diffractometer," Nucl. Instrum. Methods 127, 361−370 (1975).

2. A. W. Hewat, "D2B, a new high resolution neutron powder diffractometer at ILL Grenoble," Mater. Sci. Forum 9, 69−79 (1986).

3. P. Fischer, G. Frey, M. Koch, M. Koennecke, V. Pomjakushin, J. Schefer, R. Thut, N. Schlumpf, R. Buerge, U. Greuter, S. Bondt, and E. Berruyer, "High resolution powder diffractometer HRPT for thermal neutrons at SINQ," Physica B (Amsterdam) 276−278, 146−147 (2000).

4. W. I. F. David, W. T. A. Harrison, and M. W. Johnson, "High resolution diffraction at ISIS," Mater. Sci. Forum 9, 89−102 (1986).

5. http://flnp.jinr.ru/34/.

6. http://europeanspallationsource.se.

7. M. Russina, F. Mezei, and G. Kali, "First implementation of novel multiplexing techniques for advanced instruments at pulsed neutron sources," J. Phys.: Conf. Ser. 340, 012018 (2012).

8. K. Sköld, "A mechanical correlation chopper for thermal neutron spectroscopy," Nucl. Instrum. Methods 63, 114−116 (1968).

9. A. M. Balagurov, "High resolution Fourier diffraction at the IBR-2 Reactor," Neutron News 16, 8−12 (2005).

10. V. Glezer, "Correlation methods in time-of-flight neutron spectroscopy," Fiz. Elem. Chastits At. Yadra 4, 1125−1142 (1972).

11. R. Heinonen, P. Hiismäki, A. Piirto, H. Pöyry, and A. Tiitta, "A time-focusing Fourier chopper TOF diffractometer for large scattering angles," in Proceedings of the Neutron Diffraction Conference, Petten, 1975, RCN-234, pp.347−359.

12. J. F. Colwel, P. H. Miller, and W. L. Wittemore, "A new high-efficiency time-of-flight system," in Neutron Inelastic Scattering. Conf. Proc. (IAEA, Vienna, 1968), p. 429.

13. J. F. Colwel, S. R. Lehinan, P. H. Miller, and W. L. Wittemore, "Fourier analysis of thermal neutron time-of-flight data: A high efficiency neutron chopping system," Nucl. Instrum. Methods 76, 135−149 (1969).

14. A. C. Nunes, R. Nathans, and B. P. Schoenborn, "A neutron Fourier chopper for single crystal reflectivity measurements: Some general design considerations," Acta Crystallogr. A, Cryst. Phys., Diffr., Theor. Gen. Crystallogr. 27, 284−291 (1971).

15. A. C. Nunes, "The neutron Fourier chopper in protein crystallography," J. Appl. Crystallogr. 8, 20−28 (1975).

16. P. Hiismäki, "Inverse time-of-flight method," in Neutron Inelastic Scattering. Conf. Proc. (IAEA, Grenoble, 1972), p. 803.

17. H. Pöyry, P. Hiismäki, and A. Virjo, "Principles of reverse neutron time-of-flight spectrometry with Fourier chopper applications," Nucl. Instrum. Methods 126, 421−433 (1975).

18. R. Heinonen, P. Hiismäki, A. Piirto, H. Pöyry, and A. Tiitta, "A time focusing Fourier chopper time-of-flight diffractometer for large scattering angles," in Proceedings of the Neutron Diffraction Conference, Petten, 1975, RCN-234, pp. 347−359.

19. P. Hiismäki, V. A. Trounov, O. Antson, V. A. Kudryashev, H. Kukkonen, H. Pöyry, A. F. Shchebetov, A. Tiitta, and V. A. Ulyanov, "Experience of the Fourier TOF neutron techniques for high resolution neutron diffractometry," in Neutron Scattering in the Nineties. Conf. Proc. (IAEA, Vienna, 1985), pp. 453−459.

20. J. Schröder, V. A. Kudryashev, J. M. Keuter, H. G. Priesmeyer, J. Larsen, and A. Tiitta, "FSS—a novel RTOF-diffractometer optimized for residual stress investigations," J. Neutron Res. 2, 129−141 (1994).

21. V. A. Kudryashev, H. G. Priesmeyer, J. M. Keuter, J. Schröder, and R. Wagner, "On the shape of the diffraction peaks measured by Fourier reverse time-of-flight spectrometry," Nucl. Instrum. Methods Phys. Res., B 101, 484−492 (1995).

22. V. A. Kudryashev, H. G. Priesmeyer, J. M. Keuter, J. Schröder, and R. Wagner, "Phase errors and their influence on the RTOF-Fourier method," Nucl. Instrum. Methods Phys. Res., B 103, 517−522 (1995).

23. I. M. Frank and P. Pacher, "First experience on the high intensity pulsed reactor IBR-2," Physica B+C (Amsterdam) 120, 37−44 (1983).

24. P. Hiismäki, H. Pöyry, and A. Tiitta, "Exploitation of the Fourier chopper in neutron diffractometry at pulsed sources," J. Appl. Crystallogr. 21, 349−354 (1988).

25. V. L. Aksenov, A. M. Balagurov, V. G. Simkin, Yu. V. Taran, V. A. Trounov, V. A. Kudrjashev, A. P. Bulkin, V. G. Muratov, P. Hiismaki, A. Tiitta, and O. Antson, "The new Fourier diffractometer at the IBR-2 Reactor: Design and first results," JINR Commun. E13-92-456 (Dubna, 1992).

26. A. M. Balagurov, "High precision structural refinement from high resolution Fourier neutron powder diffraction data," Mater. Sci. Forum 166−169, 261−266 (1994).

27. A. M. Balagurov, P. Fischer, T. Yu. Kaganovich, E. Kaldis, J. Karpinski, V. G. Simkin, and V. A. Trounov, "Precision Fourier neutron diffraction study of the

high-temperature superconductor Y(^{44}Ca)Ba$_2$Cu$_4$O$_8$," JINR Commun. E14-94-415 (Dubna, 1994).

28. G. D. Bokuchava, A. V. Tamonov, N. R. Shamsutdinov, A. M. Balagurov, and D. M. Levin, "Reverse TOF neutron study of residual stresses in perforator's striker," J. Neutron Res. **9**, 255−261 (2001).

29. G. D. Bokuchava, V. L. Aksenov, A. M. Balagurov, E. S. Kuzmin, V. V. Zhuravlev, A. P. Bulkin, V. A. Kudryashev, and V. A. Trounov, "Neutron Fourier diffractometer FSD for internal stress analysis: First results," Appl. Phys. A **74**, S86−S88 (2002).

30. P. G. Radaelli, S. Hull, H. J. Bleif, and A. M. Balagurov, "Powder diffraction instruments," in *Performance of a Suite of Generic Instruments on ESS*, ESS 115-01-T (2001), pp.41−55.

31. V. L. Aksenov, A. M. Balagurov, V. G. Simkin, A. P. Bulkin, V. A. Kudrjashev, V. A. Trounov, O. Antson, P. Hiismaki, and A. Tiitta, "Performance of the high resolution Fourier diffractometer at the IBR-2 pulsed reactor," J. Neutron Res. **5**, 181−200 (1997).

32. A. M. Balagurov and V. A. Kudrjashev, "Correlation Fourier diffractometry for long-pulse neutron sources: A new concept," in 19th Meeting on Collaboration of Advanced Neutron Sources, ICANS XIX, Grindelwald, Switzerland, 2010.

33. V. A. Kudryashev, H. G. Priesmeyer, J. M. Keuter, J. Schriider, R. Wagner, and V. A. Trounov, "Optimization of detectors in time-focusing geometry for RTOF neutron diffractometers," Nucl. Instrum. Methods Phys. Res., B **93**, 355−361 (1994).

34. V. A. Kudryashev, A. P. Bulkin, V. G. Muratov, V. A. Trounov, V. A. Ulyanov, O. Antson, H. Pöyry, A. Tiitta, P. Hiismäki, A. M. Balagurov, and E. V. Serochkin, "Detection system for high-resolution diffractometers of SFINKS type," Soobshch. No.1562, LIYaF (Leningrad Inst. of Nuclear Physics, Leningrad, 1989) [in Russian].

35. E. J. Mittemeijer and U. Welzel, "The 'state of the art' of the diffraction analysis of crystallite size and lattice strain," Z. Kristallogr. **223**, 552−560 (2008).

36. V. L. Aksenov and A. M. Balagurov, "Time-of-flight neutron diffractometry," Usp. Fiz. Nauk **166**, 955−986 (1996).

37. V. B. Zlokazov and V. V. Chernyshev, "MRIA—a program for a full profile analysis of powder multiphase neutron-diffraction time-of-flight (direct and Fourier) spectra," J. Appl. Crystallogr. **25**, 447 (1992).

38. V. L. Aksenov, A. M. Balagurov, V. V. Sikolenko, V. G. Simkin, V. A. Aleshin, E. V. Antipov, A. A. Gippius, D. A. Mikhajlova, S. N. Putilin, and F. Bouree, "Precision neutron diffraction study of the high-T_c superconductor HgBa$_2$CuO$_{4+\delta}$," Phys. Rev. B: Condens. Matter **55**, 3966−3973 (1997).

39. A. M. Abakumov, V. L. Aksenov, V. A. Alyoshin, E. V. Antipov, A. M. Balagurov, D. A. Mikhailova, S. N. Putilin, and M. G. Rozova, "Effect of fluorination on the structure and superconducting properties of the Hg-1201 phase," Phys. Rev. Lett. **80**, 385−388 (1998).

40. K. A. Lokshin, D. A. Pavlov, S. N. Putilin, E. V. Antipov, D. V. Sheptyakov, and A. M. Balagurov, "Enhance-ment of T_c in Hg-1223 by fluorination," Phys. Rev. B: Condens. Matter **63**, 064511 (2001).

41. A. M. Balagurov, V. L. Aksenov, E. V. Antipov, S. N. Putilin, and D. V. Sheptyakov, "Neutron diffraction study of atomic structure of high-T_c mercury-based superconductors as a function of anion composition and external pressure," Fiz. Elem. Chastits At. Yadra **35**, 1351−1467 (2004).

42. A. M. Balagurov, V. Yu. Pomjakushin, V. G. Simkin, and A. A. Zakharov, "Neutron diffraction study of phase separation in La$_2$CuO$_{4+y}$ single crystals," Physica C (Amsterdam) **272**, 277−284 (1996).

43. V. Yu. Pomjakushin, A. A. Zakharov, A. M. Balagurov, F. N. Gygax, A. Schenck, A. Amato, D. Herlach, A. I. Beskrovnyi, V. N. Duginov, Yu. V. Obukhov, A. V. Pole, V. G. Simkin, A. N. Ponomarev, and S. N. Barilo, "Microscopic phase separation in La$_2$CuO$_{4+y}$ induced by the superconducting transition," Phys. Rev. B: Condens. Matter **58**, 12350−12354 (1998).

44. N. A. Babushkina, L. M. Belova, O. Yu. Gorbenko, A. R. Kaul, A. A. Bosak, V. I. Ozhogin, and K. I. Kugel, Nature (London) **391**, 159−161 (1998).

45. V. L. Aksenov, A. M. Balagurov, and V. Yu. Pomyakushin, "Neutron diffraction analysis of doped manganites," Usp. Fiz. Nauk **173**, 883−887 (2003).

46. A. M. Balagurov, V. Yu. Pomjakushin, D. V. Sheptyakov, V. L. Aksenov, N. A. Babushkina, L. M. Belova, O. Yu. Gorbenko, and A. R. Kaul, "A-cation size and oxygen isotope substitution effects on (La$_{1-y}$Pr$_y$)$_{0.7}$Ca$_{0.3}$MnO$_3$ structure," Eur. Phys. J. B **19**, 215−223 (2001).

47. A. M. Balagurov, I. A. Bobrikov, V. Yu. Pomyakushin, D. V. Sheptyakov, N. A. Babushkina, O. Yu. Gorbenko, M. S. Kartavtseva, and A. R. Kaul, "Effect of isotopic composition and microstructure on the crystalline and magnetic phase states in R$_{0.5}$Sr$_{0.5}$MnO$_3$," J. Exp. Theor. Phys. **106**, 528 (2008).

48. P. Scardi, M. Ortolani, and M. Leoni, "WPPM: Microstructural analysis beyond the Rietveld method," Mater. Sci. Forum **651**, 155−171 (2010).

49. A. M. Balagurov, I. A. Bobrikov, J. Grabis, D. Jakovlevs, A. Kuzmin, M. Maiorov, and N. Mironova-Ulmane, "Neutron scattering study of structural and magnetic size effects in NiO," IOP Conf. Ser.: Mater. Sci. Eng. **49**, 012021 (2013).

50. I. A. Bobrikov, A. M. Balagurov, Hu Chih-Wei, Lee Chih-Hao, Deleg Sangaa, and D. A. Balagurov, "Structural evolution in LiFePO$_4$-based battery materials: In-situ and ex-situ time-of-flight neutron diffraction study," J. Power Sources **258**, 356−364 (2014).

51. G. D. Bokuchava, V. V. Luzin, J. Schreiber, and Yu. V. Taran, "Residual stress investigations in austenitic steel samples with different degree of low cycle fatigue," Text. Microstruct. **33**, 279−289 (1999).

52. V. L. Aksenov, A. M. Balagurov, G. D. Bokuchava, A. P. Bulkin, V. A. Kudryashev, V. G. Simkin, Yu. V. Taran, V. A. Trounov, N. R. Shamsutdinov, and Yu. Shreiber, "Internal mechanical stress investigations in materials and products on the high-resolution Fou-

rier diffractometer at the IBR-2 reactor," in *Conf. RSNE-97* (Dubna, 1997), Vol. 1, p. 69 [in Russian].

53. V. A. Kudryashev, V. A. Trounov, and V. G. Mouratov, "Improvement of Fourier method and Fourier diffractometer for internal residual strain measurements," Physica B (Amsterdam) **234−236**, 1138−1140 (1997).

54. E. S. Kuzmin, A. M. Balagurov, G. D. Bokuchava, V. V. Zhuk, V. A. Kudryashev, A. P. Bulkin, and V. A. Trounov, "Detector for the FSD Fourier-diffractometer based on ZnS(Ag)/^{6}LiF scintillation screen and wavelength shifting fiber readout," J. Neutron Res. **10**, 31−41 (2002).

55. G. D. Bokuchava, A. M. Balagurov, V. V. Sumin, and I. V. Papushkin, "Neutron Fourier diffractometer FSD for residual stress studies in materials and industrial components," J. Surf. Invest.: X-ray, Synchrotron Neutron Tech. **4** (6), 879−890 (2010).

56. V. A. Trunov, V. A. Kudryashev, V. A. Ulyanov, A. P. Bulkin, V. G. Muratov, T. K. Korotkova, A. F. Shchebetov, P. Hiismäki, H. Pöyry, A. Tiitta, O. Antson, H. Mutka, H. Kukkonen, and K. Tilli, "High resolution diffractometer mini-SFINKS," Soobshch. No.1277, LIYaF (Leningrad Inst. of Nuclear Physics, Leningrad, 1987) [in Russian].

57. V. A. Drozdov, V. A. Butenko, and V. I. Prihodko, "A multi-DSP system for the neutron high resolution Fourier diffractometer," IEEE Trans. Nucl. Sci. **45**, 1928 (1998).

58. F. V. Levchanovskiy and S. M. Murashkevich, "The data acquisition system for neutron spectrometry—a new approach and implementation," in *Proc. of XXIV Intern. Symp. on Nuclear Electronics & Computing (NEC'2013)*, E10-11-136 (Dubna, 2013), pp. 176−179.

Translated by E. Kravchenko